

AperTO - Archivio Istituzionale Open Access dell'Università di Torino

The fate of calcareous pelites in collisional orogens

This is the author's manuscript

Original Citation:

Availability:

This version is available <http://hdl.handle.net/2318/1768166> since 2022-03-09T14:28:43Z

Published version:

DOI:10.1111/jmg.12568

Terms of use:

Open Access

Anyone can freely access the full text of works made available as "Open Access". Works made available under a Creative Commons license can be used according to the terms and conditions of said license. Use of all other works requires consent of the right holder (author or publisher) if not exempted from copyright protection by the applicable law.

(Article begins on next page)



DR. CHIARA GROPPPO (Orcid ID : 0000-0002-4174-6613)

Article type : Original Article

THE FATE OF CALCAREOUS PELITES IN COLLISIONAL OROGENS

Chiara Groppo¹, Giulia Rapa², Maria Luce Frezzotti², Franco Rolfo¹

¹Department of Earth Sciences, University of Torino, Torino, Italy and CNR-IGG, Torino

²Department of Earth and Environmental Sciences, University of Milano Bicocca, Milano, Italy

Running title: Prograde metamorphism of calcareous pelites

Corresponding author: Chiara Groppo (chiara.groppo@unito.it)

This article has been accepted for publication and undergone full peer review but has not been through the copyediting, typesetting, pagination and proofreading process, which may lead to differences between this version and the [Version of Record](#). Please cite this article as [doi: 10.1111/JMG.12568](https://doi.org/10.1111/JMG.12568)

This article is protected by copyright. All rights reserved

Abstract

Although calcareous pelites are important constituents of sediments involved in orogenic processes, their prograde metamorphism is significantly less studied than that of pure pelites with negligible amounts of modal calcite. This paper presents mineral equilibria modeling in the system $\text{MnO}-\text{Na}_2\text{O}-\text{K}_2\text{O}-\text{CaO}-\text{FeO}-\text{MgO}-\text{Al}_2\text{O}_3-\text{SiO}_2-\text{TiO}_2-\text{H}_2\text{O}-\text{CO}_2$, with the aim of constraining the prograde evolution of calcareous pelites in collisional orogenic settings.

A suite of model bulk rock compositions is used to investigate the influence of different proportions of calcite in the protolith on: (i) the equilibrium assemblages at different pressure, temperature and fluid composition (P - T - $X(\text{CO}_2)$) conditions; (ii) the melt-fertility, and (iii) the fluid evolution and the main decarbonation reactions occurring during prograde metamorphism of calcareous pelites. In spite of being purely theoretical, the reliability of the modeling is tested by comparing the predicted assemblages with those observed in a wide set of natural samples from the Himalayan metamorphic core. Comparison between the predicted and the modelled assemblages demonstrates that even a small amount of calcite in the calcareous pelitic protoliths has a strong influence on the final mineral assemblages and compositions, with potential effects on their melt-productivity. Specifically, it appears that up to $\sim 800^\circ\text{C}$, the melt productivity of calcic metapelites remains low, and melt production occurs gradationally because it is mostly controlled by continuous biotite dehydration melting reactions, rather than by muscovite breakdown. Moreover, the study demonstrates that calcareous pelites could be non-negligible CO_2 -source rocks in orogenic settings, and that in such contexts, an internal buffered behavior is likely for most of them.

Key-words

Calcareous pelites, phase equilibria modelling, melt fertility, decarbonation processes, Himalaya

1. INTRODUCTION

Calcareous pelites are important constituents of sedimentary sequences deposited in passive margin settings through time; their mineralogical composition is transitional between pure pelites (dominated by clay minerals, quartz and feldspars and virtually free of carbonates) and marls (consisting of a mixture of pelitic and carbonatic components). The amount of carbonates in calcareous pelites is generally lower than 10 vol%, whereas higher proportions of carbonates (10–50 vol%) occur in argillaceous marls and marls *sensu stricto* (Pettijohn, 1957). Calcareous pelites can be therefore adequately described by adding the CaO and CO₂ components to the (Na₂O)–K₂O–FeO–MgO–Al₂O₃–SiO₂–H₂O (N)KFMASH system commonly used to describe pure pelites.

During prograde metamorphism of calcareous pelites, it is expected that calcium-rich minerals develop from the reactions between calcite and the silicate assemblage, leading ultimately to the complete disappearance of calcite. Among these calcium-rich minerals, the most typical ones are plagioclase and zoisite/clinozoisite. Margarite, scapolite, grossular-rich garnet and minor calcic-amphibole and/or clinopyroxene can also appear, depending on the amount of calcite originally present in the protolith, on the bulk rock composition and on the pressure–temperature (P–T) metamorphic conditions (e.g. Ferry, 1976, 1983a,b, 1992; Hewitt, 1973; Menard & Spear, 1993; Yardley, 1977; Zen 1981). Commonly occurring in low modal amounts, most of these calcium-rich minerals are not particularly evident on the hand specimen, therefore the metamorphic products of calcareous pelites might appear trivial with respect to those of both pure metapelites (characterized by the widespread occurrence of aluminum-rich index minerals, such as staurolite and aluminosilicates) and of marls (which are transformed into calc-schists or calc-silicate rocks). In the field, metamorphosed calcareous pelites are often neglected in favor of more appealing, index minerals -bearing lithologies; even when collected, they are rarely investigated in detail due to the complexity of the Na₂O–K₂O–CaO–FeO–MgO–Al₂O₃–SiO₂–H₂O–CO₂ (NKC FMASH–H₂O–CO₂) system.

Because of these reasons, prograde metamorphism of calcareous pelites is significantly less studied than metamorphism of pure pelites (e.g. Bucher & Grapes, 2011). CaO and Na₂O are routinely considered in the pelitic system, but CO₂ is generally ignored. A quantitative investigation of phase relations in the NKC FMASH system was performed at first by Vance & Holland (1993): in their calculations they included Na₂O and CaO in white mica and garnet, but did not consider plagioclase. Worley & Powell (1998) further explored the influence of CaO and Na₂O in the pelitic system by incorporating CaO in garnet, and both Na₂O and CaO in white micas and plagioclase; they demonstrated that singularities commonly occur along univariant equilibria involving Ca–Na solid solutions, thus highlighting the complexity of the modeling in such a system. Further development of efficient software for

thermodynamic calculations allowed considering additional important minor components such as MnO, TiO₂ and/or Fe₂O₃ (e.g. White, Powell, & Holland, 2001; White, Powell, & Holland, 2007; White, Powell, Holland, Johnson, & Green 2014; White, Powell, & Johnson, 2014) and understanding their influence on the evolution of mineral assemblages in the pelitic system. The occurrence of low amounts of carbonates in the pelitic protoliths was generally ignored and phase relations for calcareous pelites have been poorly explored so far. Notable exceptions are those of Thompson (1975) and Ferry (1976, 1983a,b), whose isobaric T–X(CO₂) grids calculated in the KCMAS–H₂O–CO₂ and KCFMAS–H₂O–CO₂ systems, respectively, represent valuable attempts of constraining prograde metamorphism of calcareous pelites. Zen (1981) also proposed an elegant treatment of phase relations in slightly calcic pelitic rocks, but did not consider Na₂O and CO₂ components. More recently, Nabelek & Chen (2014) investigated the role of carbonates (siderite-rhodochrosite solid solution) in the nucleation and growth of garnet in graphitic schists, providing convincing evidence of the importance of considering CO₂ when studying metamorphism of metapelites, even if carbonates are no more present in the studied rocks.

In this paper we use mineral equilibria modeling in the system MnO–Na₂O–K₂O–CaO–FeO–MgO–Al₂O₃–SiO₂–TiO₂–H₂O–CO₂ (MnNKCFMAST–H₂O–CO₂) to constrain the prograde evolution of calcareous pelites in Barrovian-type collisional orogenic settings. A suite of model bulk rock compositions has been selected in order to test the influence of different proportions of calcite in the protolith on: (i) the equilibrium assemblages at different P–T–X(CO₂) conditions; (ii) the melt-fertility of calcareous pelites, and (iii) the fluid evolution and the main decarbonation reactions occurring during prograde metamorphism. In spite of being purely theoretical, the reliability of the modeling is tested by comparing the predicted assemblages with those observed in a wide set of natural samples from the Himalayan metamorphic core.

Comparison between the predicted and the modelled assemblages in calcic metapelites demonstrates that even a small amount of calcite in the pelitic protoliths has a strong influence on the final mineral assemblages and compositions, with potential effects on their melt-productivity. Moreover, the study demonstrates that calcic metapelites could be non-negligible CO₂-source rocks in orogenic settings, and that in such contexts, an internal buffered behavior is likely to occur for most of them.

2. CALCIC METAPELITES FROM THE HIMALAYAN METAMORPHIC CORE

2.1 Observed lithologies

The Lesser and Greater Himalayan Sequences (LHS and GHS) exposed in the metamorphic core of the Himalayan belt mostly consist of meta-sediments deposited during the Proterozoic (LHS: Paleoproterozoic to Mesoproterozoic; GHS: Neoproterozoic) on the northern edge of the Indian passive margin, and later

involved in the India-Asia continental collision that started 50–55 Ma ago and led to the formation of the Himalayan orogen (e.g. Goscombe, Gray, & Foster, 2018; Kohn, 2014). These meta-sediments derive from protoliths ranging in composition from pure pelites to calcareous pelites, with minor intercalations of marls and impure limestones (e.g. Dyck et al., 2018; Hodges, 2000; Pearson & De Celles, 2005; Upreti, 1999), and experienced Barrovian-type metamorphism at variable peak P–T conditions (e.g. Kohn, 2014; Rapa, Mosca, Groppo, & Rolfo, 2018; Rolfo, Groppo, & Mosca, 2015). From the lower to the upper structural levels, average peak P–T conditions for the LHS in central-eastern Nepal can be summarized as follows (see the extended review by Goscombe et al., 2018): 450–500°C, 5–7 kbar (biotite zone), 500–550°C, 7–9 kbar (garnet zone), 560–600°C, 7–10 kbar (garnet + staurolite zone). An inverted metamorphic gradient also characterizes the Lower-GHS (also known as Main Central Thrust Zone; e.g. Mosca, Groppo, & Rolfo, 2012), with average peak P–T conditions, from the lower to the upper structural levels, in the range: 600–650°C, 7–11 kbar (staurolite zone), 610–670°C, 7–10 kbar (kyanite zone), 650–720°C, 6–9 kbar (sillimanite + kyanite zone). The Upper-GHS experienced peak metamorphism at higher temperatures and lower pressures, resulting in a widespread anatexis. Average peak P–T conditions for the Upper-GHS are: 670–730°C, 5–8 kbar (garnet + sillimanite + K-feldspar zone) and 700–780°C, 4–7 kbar (garnet + cordierite + sillimanite + K-feldspar zone).

Over 15 years of extensive fieldwork in central-eastern Nepal allowed us to gather a very large dataset (i.e. few thousands) of meta-sedimentary samples from both the LHS and GHS. Focus of this paper are the metamorphic products of calcareous pelites (original calcite content <10 vol%; called hereafter calcic metapelites), which are widespread in both the LHS and GHS and occur as intercalations within pure metapelites. They consist of muscovite and/or biotite, ± garnet-bearing, schists or gneisses, with a total amount of micas generally higher than 15–20 vol%. These lithologies always contain variable amounts of calcium-rich minerals, among which the most common are plagioclase, zoisite/clinozoisite and scapolite; minor amounts of calcite are locally preserved, especially as inclusions within garnet. In most cases, biotite is the main mafic mineral, often associated with minor amounts of almandine-rich garnet; calcic amphibole can be locally present in some calcic metapelites, whereas clinopyroxene is systematically absent. Most of the calcium-rich minerals in calcic metapelites (plagioclase, zoisite/clinozoisite, scapolite) are not always easily recognizable at the outcrop scale. As a consequence, calcic metapelites can be mistaken in the field for common metapelites (to which they are associated) especially in the case of garnet-bearing schists. By contrast, they can be easily distinguished from the metamorphic products of marls (i.e. calcschists and calc-silicate gneisses), due to the significant lower amounts of calcite at low metamorphic grade and to the significant higher amounts of biotite and the lack of clinopyroxene at medium to high metamorphic grade.

Table S1 summarizes the main petrographic features of a representative selection (i.e. 30 samples) of calcic metapelites from our collection. Based on their mineral assemblages, five main lithologic types have been identified and are hereafter briefly described (see also Rolfo, Groppo, & Mosca, 2017). The studied samples are exposed at different structural levels, in both the LHS and the GHS (detailed location is provided in Figure S1 and Table S1). Mineral abbreviations in the text, figures and tables are according Whitney & Evans (2010).

2.1.1 Type 1: Ca-rich plagioclase + garnet \pm zoisite -bearing two-micas schists (LHS) or biotitic gneisses (GHS)

This is the most common type of calcic metapelite in our collection and includes samples from both the LHS (garnet + staurolite zone) and the Lower-GHS (kyanite and sillimanite + kyanite zones).

In the LHS, these rocks are two-micas schists characterized by the occurrence of garnet + plagioclase \pm zoisite porphyroblasts (Figure 1a,b). The main foliation is always defined by muscovite + biotite; biotite locally also occurs as porphyroblasts statically overgrowing the main foliation. Garnet porphyroblasts are generally poikiloblastic, and commonly include a rotated internal foliation defined by quartz, ilmenite, \pm zoisite/clinozoisite (Figure 1b); in few samples (99–45; 17a–29), calcite relics are preserved as corroded inclusions in garnet, suggesting that garnet grew through a decarbonation reaction. Ca-rich plagioclase generally occurs as large (mm- to pluri-mm) porphyroblasts statically overgrowing the main foliation (Figure 1b) and commonly shows a patchy zoning and/or optically visible exolutions. If present, zoisite porphyroblasts are pre- to syn-kinematic with respect to the main foliation and are partially replaced by plagioclase (10–38a; Figure 1a).

In the GHS, this lithology consists of garnet + plagioclase -bearing biotitic schists or gneisses characterized by the anomalous abundance of plagioclase with respect to the associated metapelites (Figure 1c–g). The main foliation is mainly defined by biotite, with minor amounts of white mica in few samples only (99–15; 18a–9b; Figure 1d). Garnet is generally poikiloblastic and/or with a skeletal habit, pre- to syn-kinematic with respect to the main foliation (Figure 1c,d) or, more rarely, fine-grained and idioblastic (Figure 1e–g). It systematically includes quartz and zoisite/clinozoisite, \pm plagioclase and biotite. Few samples (99–15; 18a–9b) still preserve calcite concentrated in lens-like domains; in this case, garnet is systematically associated with calcite-rich domains and includes corroded calcite relics (Figure 1d). Ca-rich plagioclase either occurs as large porphyroblasts overgrowing the main foliation (e.g. 13–69; 17a–11; 18a–9b; Figure 1d,g) or as fine- to medium-grained granoblasts in the matrix (e.g. 99–15; 06–27; 12–53a; 16–51; 18a–9a; 18a–14a; Figure 1c,e,f) and it is often patchy zoned. Zoisite/clinozoisite porphyroblasts are less frequent (18a–9a) and mostly aligned to the main foliation (Figure 1f).

2.1.2 Type 2: Ca-rich plagioclase \pm zoisite/clinozoisite -bearing two-micas schists (LHS) or biotitic schists (GHS)

These rocks are exposed in both the LHS (garnet + staurolite zone) and Lower-GHS (kyanite and sillimanite + kyanite zones) and show a relatively simple mineral assemblage.

In the LHS, they consist of two-micas schists characterized by plagioclase abundance significantly higher than in normal metapelites (e.g. 08–32). Plagioclase is rich in the anorthite component, showing relatively high relief and birefringence, and it is commonly patchy zoned. Fine-grained zoisite/clinozoisite also occurs in the equilibrium assemblage.

In the Lower-GHS, these rocks are mostly biotitic gneisses with minor amounts of muscovite and contain significant amounts of Ca-rich plagioclase (Figure 1h). Minor amounts of K-feldspar occur at the uppermost structural levels (sillimanite + kyanite zone).

2.1.3 Type 3: Garnet + scapolite -bearing two-micas schists or biotitic gneisses (GHS)

This lithology is exclusively exposed in the lowermost structural levels of the Lower-GHS (staurolite and kyanite zones) and consists of two-micas schists or biotitic gneisses characterized by the co-existence of garnet and scapolite (Figure 2a–d). These rocks are locally banded (e.g. 14–38a), with garnet + scapolite -rich layers alternated to clinozoisite + scapolite -rich layers. The main foliation is always defined by biotite; muscovite occurs only in few samples (13–42; 13–38a; 17b–21; Figure 2a,c) and it is always less abundant than biotite. Garnet is always porphyroblastic, poikiloblastic or with a skeletal habit, and mostly includes quartz, plagioclase and clinozoisite (Figure 2a–d), more rarely relict calcite (13–38a; 15a–46). Scapolite is either dispersed in the matrix (13–42; 15a–46; Figure 2d) or concentrated in lens-like domains (13–38a; 14–38a; 16–26; 17b–21; Figure 2a–c) together with garnet. Ca-rich plagioclase mostly appears to be in equilibrium with scapolite. Clinozoisite is observed in most of the samples, and occurs as fine-grained crystals in equilibrium with scapolite.

2.1.4 Type 4: Scapolite -bearing biotitic gneisses (GHS)

This lithology is exposed in the uppermost structural levels of the Lower-GHS (sillimanite + kyanite zone). It differs from type 3 because it lacks garnet porphyroblasts and it commonly contains K-feldspar (Figure 2e–f). The equilibrium assemblage is relatively simple and mostly consists of quartz, plagioclase \pm K-feldspar, biotite, scapolite and minor clinozoisite. The main, gneissic, foliation is defined by biotite; few muscovite occurs as a retrograde phase overgrowing the main foliation. Scapolite is locally quite abundant

and it is concentrated in the quartz-feldspathic domains, showing equilibrium relationships with plagioclase (Figure 2e–f).

2.1.5 Type 5: Amphibole + garnet -bearing two-micas schists or biotitic gneisses (LHS and GHS)

This lithology is exposed in the LHS (garnet + staurolite zone) and in the lowermost structural levels of the Lower-GHS (kyanite zone).

In the LHS, both two-micas schists and biotitic gneisses are exposed, characterized by the co-existence of garnet and calcic amphibole. The two-micas schists (06–8; 15b–25; 17a–25) are fine-grained and the main foliation is defined by muscovite + biotite \pm chlorite. Garnet porphyroblasts, locally with a skeletal habit, are syn- to post-kinematic with respect to the main foliation; calcic amphibole is colorless and occurs in mm-sized porphyroblasts overgrowing the main foliation (Figure 2g). Generally, amphibole is modally scarce. The biotitic gneisses show a poorly pervasive foliation defined by biotite-rich discontinuous layers alternated to quartzo-feldspathic domains. Garnet porphyroblasts have a skeletal habit; calcic amphibole is green and occurs either in aggregates overgrowing the main foliation and associated with chlorite (15a–19b) or as fine-grained crystals aligned to the main foliation (99–23).

In the Lower-GHS, this lithology is represented by biotitic gneisses dominated by quartzo-feldspathic layers. Garnet occurs as mm-sized poikiloblasts, and it is in textural equilibrium with a pale-green calcic amphibole (e.g. 15a–47b; Figure 2h).

2.2 Measured bulk compositions and the nature of protoliths

Bulk-rock compositions of 5 samples of calcic metapelites, 15 samples of calc-silicate rocks and 3 samples of impure marbles from both LHS and GHS (Table 1a,b) were acquired by inductively coupled plasma mass spectrometry (ICP-MS) analysis by ALS Chemex, Vancouver, Canada. These compositions are compared with already published bulk-rock compositions of metapelites *sensu stricto* (11 samples; Groppo, Rolfo, & Lombardo, 2009; Rapa, Groppo, Mosca, & Rolfo, 2016) collected from similar structural levels within LHS and GHS (Table 1c), as well as with the following average pelite and metapelite compositions from the literature (Table 1d): NASC, "North American Shale Composite" (Gromet, Dymek, Haskin, & Korotev, 1984), PAAS, "Post-Archean Australian Shale" (Taylor & McLennan, 1985), average of about 100 analyses of pelites and slates (Ague, 1991), average of pelagic clays (Carmichael, 1989), average of Archean, Proterozoic and Phanerozoic Shales (Condie, 1993), average of low-grade metapelites from the Littleton Fm. (Shaw, 1956), average of amphibolite-facies metapelites (Ague, 1991).

Altogether, the bulk-rock compositions of these meta-sediments define relatively narrow compositional ranges in terms of major components (Figure 3) and further confirm the existence of a

continuous transition from pure pelites to calcareous pelites, marls and impure limestones. The CaO contents are extremely variable, ranging from 20–30 wt% (53–77 mol%) in impure marbles to 2–6 wt% (3–7 mol%) in calcic metapelites, to 0–2.5 wt% (0–3 mol%) in pure metapelites. Normalized to a SiO₂- and CaO -free basis, the average Al₂O₃ and FeO_{tot}+MgO contents of calcic metapelites are in the range 40–47 mol% (average 44 mol%) and 38–45 mol% (average 41 mol%), respectively; K₂O and Na₂O are more variable, ranging between 6–12 mol% (average 9 mol%) and 2–7 mol% (average 4 mol%), respectively. The average FeO_{tot}/(FeO_{tot}+MgO) ratio is 0.6. Metasediments derived from marls show similar compositional ranges, with Al₂O₃ = 34–46 mol% (average 39 mol%), FeO_{tot}+MgO = 32–51 mol% (average 41 mol%), K₂O = 6–19 mol% (average 11 mol%) and Na₂O = 3–8 mol% (average 6 mol%).

These relatively homogenous bulk-rock compositions reflect similar protolith compositions in terms of silicic constituents, but different original amounts of calcite. Starting from the bulk-rock compositions, approximated protolith's mineralogical compositions have been reconstructed according to the following assumptions: (i) CaO from silicate fraction (CaO* in Table 1) is equivalent to Na₂O (e.g. Hofer, Wagreich, & Neuhuber, 2013; McLennan, Hemming, McDaniel, & Hanson, 1993) and is incorporated in anorthite; the remaining CaO is incorporated in calcite; (ii) chlorite is the only mafic mineral in the protolith; (iii) albite incorporates all the Na₂O. The modal proportions of the protolith's minerals have been obtained by applying the least square method (freeware application available on demand; Godard, 2009) and using end-member compositions and molar volumes for kaolinite, illite, clinocllore, daphnite, albite, anorthite, quartz and K-feldspar. The result is considered satisfactory if the residuals (i.e. molar bulk composition of the protolith's minerals - molar bulk rock composition) are close to zero. Following this approach, it emerges that all the analysed metasediments derive from protoliths originally containing quartz, clay minerals (illite ± kaolinite), chlorite and feldspars (plagioclase ± K-feldspar) in different proportions, with calcite amounts in the range 1–10 vol% for calcic metapelites, 12–47 vol% for metasediments derived from marls and 63–85 vol% for impure marbles (Figures 3d and 4, Table 1a,b). Protoliths of the analysed metapelites did not contain calcite, except for one sample (14–24; Figure 4b, Table 1c), which contained 3 vol% of calcite. Most of the analysed meta-sediments reflect moderate degree of weathering (i.e. K-feldspar is still preserved); higher degrees of weathering are suggested by few of them, containing kaolinite rather than K-feldspar (Figure 4a,b). The average pelite and metapelite compositions taken from the literature point to calcite-free protoliths, except for NASC ("North American Shale Composite": Gromet et al., 1984), which contained 4 vol% of calcite (Figures 3d and 4c, Table 1d).

3. METHODS

3.1 Model bulk compositions

Model bulk-rock compositions used to calculate the different sets of $P/T-X(\text{CO}_2)$ pseudosections were obtained by adding different amounts of calcite to a standard pelite composition, representative of the average of metapelites in the LHS and GHS. The starting pelite composition (Cal0) is (mol%): SiO_2 72.2, TiO_2 0.7, Al_2O_3 11.1, FeO 6.2, MgO 4.3, MnO 0.1, CaO 1.0, Na_2O 1.9, K_2O 2.5 (Table 2), corresponding to an approximate protolith consisting of quartz (31 vol%), illite (22 vol%), chlorite (18 vol%), plagioclase (20 vol%) and K-feldspar (9 vol%) (Figure 3e and 4d, Table 2). It is noteworthy that Cal0 composition is very similar to the average of about 100 analyses of pelites and slates, as well as to the average of amphibolite-facies metapelites published by Ague (1991) (i.e. compositions 3 and 9 in Figures 3 and 4c).

Model compositions Cal3, Cal6 and Cal9 were calculated adding 3, 6 and 9 vol% of calcite to Cal0 (Table 2), respectively. Bulk compositions derived from the addition of other carbonates (e.g. dolomite, ankerite) beside calcite are not considered in this paper, which is specifically referred to calcic metapelites originally containing small amounts of calcite. Cal3 composition is very similar to the NASC composition ("North American Shale Composite": Gromet et al., 1984, composition 1 in Figures 3 and 4c), thus confirming that calcareous pelites are important components of upper crustal sediments.

Model compositions Cal0 to Cal9 have a $\text{MgO}/(\text{MgO}+\text{FeO})$ ratio of 0.4. The influence of variable Mg/Fe ratios was explored using an additional set of model compositions with a $\text{MgO}/(\text{MgO}+\text{FeO})$ ratio of 0.6 (_highMg compositions in Table 2). Moreover, because Na_2O is the most variable (compared to its maximum amount) among the major components in the analysed metasediments (Figure 3c), ranging from 0.5 to 3.0 mol%, its influence was investigated using two additional sets of model compositions, representing Na_2O -depleted and Na_2O -enriched compositions obtained by decreasing and increasing the Na_2O amount to 0.5 and 3.0 mol%, respectively (Figures 3c and 4d). Bulk compositions depleted in Na_2O (_lowNa compositions in Table 2) correspond to protoliths with lower amounts of feldspars and higher amounts of illite (i.e. moving toward pure pelites), whereas those enriched in Na_2O (_highNa compositions in Table 2) are representative of protoliths with more than 35–40 vol% of feldspars (i.e. moving toward arkoses) (Figures 3e and 4d). Moreover, because CaO from the silicate fraction (CaO^* in Table 2) is set as equivalent to Na_2O (see Section 2.2), Na_2O -depleted and Na_2O -enriched compositions respectively contain more and less calcite with respect to the starting bulk compositions (see Table 2 and Fig. 3c and Fig. 4d).

A total of 16 model compositions were therefore used to calculate the $P/T-X(\text{CO}_2)$ pseudosections (Table 2). Although they are probably not exhaustive, these compositions can be nevertheless considered as representative of the compositional variations of most of the calcic metapelites exposed in the LHS and GHS (see section 5.1, for a comparison between the modeled and the observed mineral assemblages).

3.2 P/T–X(CO₂) projections

Two P/T–X(CO₂) projections were calculated in the simplified NCKMAS–H₂O–CO₂ and NCKFAS–H₂O–CO₂ sub-systems, respectively, along a P/T gradient representative of common prograde evolution during Barrovian metamorphism in a convergent setting. The P/T–X(CO₂) projections were calculated in the range 400–700°C (5.7–10 kbar) and X(CO₂) = 0.00–0.25; higher values of X(CO₂) were not considered compatible with an internally buffered P/T–X(CO₂) evolution of calcic metapelites originally containing less than 10 vol% of calcite. The grids were calculated using Perplex 6.8.6 (version March 2018; Connolly, 1990, 2009), the internally consistent thermodynamic dataset of Holland & Powell (2011) (ds62) and the equation of state for H₂O–CO₂ binary fluid of Holland & Powell (1998). Solid solution models were considered for garnet (Ca–Fe: White et al., 2014a,b), plagioclase (Na–Ca: Newton, Charlu, & Kleppa, 1980) and scapolite (Na–Ca: Kuhn, Reusser, Powell, & Günther, 2005), but not for white mica. More specifically, margarite was not included in the calculation of the projections because it has never been observed in calcic metapelites from LHS and GHS, whereas muscovite and paragonite have been considered as pure end-members. The consequence of this simplification is that the stability field of muscovite predicted by the projections is smaller than that predicted by the pseudosections (and viceversa for K-feldspar). For mafic minerals, the Mg and Fe end-members were considered for chlorite (clinochlore, daphnite), biotite (phlogopite, annite) and clinopyroxene (diopside, hedenbergite). Amphibole and staurolite end-members were not included in the calculation for sake of simplicity, although they were considered in the P/T–X(CO₂) pseudosections and are predicted to be stable for some of the model bulk compositions (see section 4.2). Therefore, amphibole- and staurolite-bearing equilibria will not be discussed in detail. Calcite, K-feldspar, quartz and zoisite were considered as pure phases.

The approach is similar to that used by Groppo, Rolfo, Castelli, & Connolly (2013) in the CFAS–H₂O–CO₂ system, and to that described by Groppo, Rolfo, Castelli, & Mosca (2017) and Rapa et al. (2017) in the NCKMAS–H₂O–CO₂ and NCKFMAST–H₂O–CO₂ systems respectively, although activity modified end-members were used in those papers.

3.3 P/T–X(CO₂) pseudosections

A set of 16 P/T–X(CO₂) pseudosections were calculated using the model bulk compositions discussed in section 3.1, along the same P/T gradient and in the same P/T–X(CO₂) range used for the projections. For temperatures higher than ~ 650–670°C, the modeled assemblages could be metastable with respect to melt, that was not included in the calculations. However, along the considered P/T gradient and for pure

metapelites, significant amounts of melt only appear at $T > 750^{\circ}\text{C}$, through muscovite dehydration melting (White et al., 2001).

The pseudosections were calculated in the $\text{MnNKCFAST-H}_2\text{O-CO}_2$ system using the same PerpleX version (6.8.6), thermodynamic dataset and equation of state for fluid used for the $\text{P/T-X(CO}_2\text{)}$ projection. Fluid was considered as a saturated phase; this constraint implies that a binary $\text{H}_2\text{O-CO}_2$ fluid phase is stable in the whole $\text{P/T-X(CO}_2\text{)}$ region of interest. The following solution models were used: garnet, chlorite, chloritoid, staurolite, white mica, biotite and ilmenite (White et al., 2014a,b), amphibole and clinopyroxene (Green et al., 2016), scapolite (Kuhn et al., 2005), plagioclase (Newton et al., 1980), K-feldspar (Thomson & Hovis, 1979), carbonate (i.e. Ca-Mg-Mn-Fe carbonate with calcite structure; Massonne, 2010) and dolomite (Holland & Powell, 1998). Quartz, zoisite, kyanite, rutile and titanite were considered as pure phases. It is noteworthy that the simplifications introduced in the calculation of the $\text{P/T-X(CO}_2\text{)}$ projections as concerning white mica (i.e. exclusion of margarite; muscovite and paragonite treated as pure end-members), are overcome in the calculation of the $\text{P/T-X(CO}_2\text{)}$ pseudosections thanks to the use of the complete K-Na-Ca white mica solution model.

4. RESULTS

4.1 $\text{P/T-X(CO}_2\text{)}$ projections

The $\text{NKCMAST-H}_2\text{O-CO}_2$ and $\text{NKCFAS-H}_2\text{O-CO}_2$ (in the following referred to as NKCMAST and NKCFAS , implicitly considering H_2O and CO_2) projections (Figure 5) represent the backbone for the calculation of the $\text{P/T-X(CO}_2\text{)}$ pseudosections, even though only small segments of univariant reactions may be seen by a given rock composition (i.e. only small segments of univariant reactions may have a multivariant equivalent in the pseudosections) (e.g. Elmer, White, & Powell, 2006; Worley & Powell, 1998).

The MgO and FeO -free NCAS , KCAS and NKCAS equilibria are the same for the two sub-systems. In the $\text{P-T-X(CO}_2\text{)}$ range of interest, there is one NCAS (I1: $[\text{Grs}]$) and three NKCAS (I2: $[\text{Grs}, \text{Scp}]$, I3: $[\text{Grs}, \text{Pg}]$, I4: $[\text{Qz}, \text{Scp}]$) invariant points. Five NCAS (1 to 5), one KCAS (6) and five NKCAS (7 to 11) univariant equilibria emanate from these invariant points (Figure 5). Relevant for the following discussion are equilibria 2 ($\text{Cal} + \text{Pl} + \text{Zo} = \text{Scp}$), 10 ($\text{Cal} + \text{Mu} + \text{Pl} + \text{Qz} = \text{Kfs} + \text{Scp}$) and 11 ($\text{Mu} + \text{Qz} + \text{Scp} = \text{Kfs} + \text{Pl} + \text{Zo}$).

Different invariant and univariant equilibria are predicted for the CMAS and CFAS sub-systems. In the CMAS sub-system no invariant points are modeled, and three univariant equilibria (12 to 14) are predicted in the $\text{P-T-X(CO}_2\text{)}$ range of interest. In the CFAS sub-system, there is one invariant point (I5: $[\text{An}, \text{Mei}]$), from which emanate six univariant curves (13 to 18). Two of them (13 and 17) show a singularity (Figure 5), at which the stoichiometric coefficient of calcite becomes zero. Equilibria 13 and 14

are modelled in both the CMAS and CFAS sub-systems (Figure 5). Relevant for the following discussion is equilibrium 13a ($\text{Cal} + \text{Clc/Dph} + \text{Qz} + \text{Zo} = \text{Grt}$).

In the NCMAS sub-system there is one invariant point (I6: [Grt, Pg]), from which emanate two NCMAS univariant equilibria (19 and 20), in addition to the degenerate NCAS and CMAS equilibria 2 and 14. An additional NCMAS univariant curve 21 is predicted for very low $X(\text{CO}_2)$ values, which has a FeO-counterpart in the NCFAS sub-system. In the NCFAS sub-system, there is one invariant point (I7: [Scp, Hd]) from which three NCFAS univariant curves (21 to 23) emanate, in addition to the degenerate NCAS and CFAS equilibria 1 and 13a, respectively. One of the NCFAS univariant equilibria (21) shows a singularity (Figure 5), at which the stoichiometric coefficient of calcite becomes zero.

Two invariant points (I8: [Grt, Mu], I9: [Kfs, Di]) and nine univariant equilibria (24 to 32) are modeled in the KCMAS sub-system. One of the invariant point (I8) and some of the univariant equilibria (27 to 32) have their equivalent in the KCFAS sub-system. In the KCFAS sub-system, three additional invariant points (I9: [Grt, Hd], I10: [Dph, Hd], I11: [Dph, Mu]) and nine additional univariant equilibria (33 to 41) are modelled. Equilibria 32 and 38 show one and two singularities, respectively (Figure 5), at which the stoichiometric coefficients of calcite (32 and 38) and K-feldspar (38) become zero. Relevant for the following discussion is equilibrium 30 ($\text{Cal} + \text{Clc/Dph} + \text{Mu} + \text{Qz} = \text{Phl/Ann} + \text{Zo}$).

In the NKCMAS sub-system, three invariant (I12: [Clc, Grt, Mu, Pg], I13: [Di, Grt, Kfs, Qz], I14: [Di, Grt, Kfs, Pg]) and ten univariant (42 to 51) equilibria are modeled which don't have counterparts in the NKCFAS sub-system. In the NKCFAS sub-system there are two invariant points (I15: [Grt, Hd, Mu, Scp], I16: [Dph, Hd, Kfs, Scp]) and six univariant equilibria (52 to 57). Relevant for the following discussion is equilibrium 51 ($\text{Phl} + \text{Qz} + \text{Scp} = \text{Di} + \text{Kfs} + \text{Pl} + \text{Zo}$).

4.2 P/T-X(CO₂) pseudosections

P/T-X(CO₂) pseudosections calculated for the model compositions Cal0, Cal3, Cal6 and Cal9 allow to investigate the influence of variable amounts of calcite in the protolith on the predicted mineral assemblages and fluid composition. In the following, the results of thermodynamic modeling (Figures 6 and 7) are discussed only for dolomite and ankerite –free fields, these carbonates being systematically absent from the observed natural samples, as well as from the protoliths reconstructed in section 2.2. Phase equilibria modelling results are summarized in Figures 6 and 7; details on field assemblages, mineral abundances and plagioclase composition are given in Figures S2–S6.

4.2.1 Cal0

The P/T-X(CO₂) pseudosection modelled for Cal0 (Figures 6a, S2a and S3a) is dominated by 3- and 4-variant fields, with minor 2- and 5-variant fields. The calcite stability field is limited to T < 480°C and the predicted amounts of calcite are lower than 1 vol%.

Muscovite is predicted to be stable in the entire P–T–X(CO₂) range of interest (Figure 6a) and its modal amount is maximum (>30 vol%) at lower T and minimum (~ 10 vol%) at intermediate temperatures, where it coexists with paragonite. At T > 600°C its modal amount is slightly higher than 20 vol%. Biotite modally increases up-T, with a maximum of 20–22 vol% at 500–540°C. Paragonite is predicted to be stable at 470–600°C, whereas chlorite mostly disappears at T > 500°C (Figure 6a). Garnet appears in very low amounts at about 460°C, but its abundance exceeds 1 vol% (i.e. it becomes evident) only at T > 530°C (Figures 6a). At this temperature, garnet composition is approximately Alm₅₇Sps₁₀Prp₆Grs₂₆ and it varies with increasing temperature up to Alm₇₃Sps₂Prp₁₈Grs₇ at T > 600°C. Up to 14 vol% of albite is stable at T < 500°C, whereas plagioclase appears at T > 540°C; a plagioclase-absent field is therefore predicted in the temperature range 500–540°C (Figure 6a). Plagioclase is an oligoclase, with anorthite content decreasing up-T from An₃₀ to An₁₈. Very small amounts of zoisite are predicted at T < 550°C, with a maximum of 2 vol% in the plagioclase-absent field.

4.2.2 Cal3

The P/T–X(CO₂) pseudosection modelled for Cal3 (Figures 6b, S2b and S3b) is similar to that modeled for Cal0; it is mostly dominated by calcite-absent fields, calcite (up to 4 vol%) being limited to T < 490°C. The transition from calcite-bearing to calcite-absent assemblages is marked by a narrow 3-variant field corresponding to the KCMAS/KCFAS univariant reaction 30 (Cal + Clc/Dph + Mu + Qz = Phl/Ann + Zo) and, at higher temperatures, by a narrow 2-variant field corresponding to the CMAS/CFAS univariant reaction 13 (Cal + Clc/Dph + Qz + Zo = Grt) (Figure 5). Field assemblages and mineral compositions in the calcite-absent field are mostly independent from X(CO₂), as expected. The sequence of predicted prograde assemblages is similar to that already discussed for Cal0, but with significant different proportions of micas and calcium-bearing phases.

Muscovite is always stable (Figure 6b) but its modal amount does not exceed 15–18 vol% in most of the P–T–X(CO₂) range of interest, whereas biotite distribution is similar to that modelled for Cal0 (i.e. mostly in the range 15–23 vol%). Albite reaches a maximum modal amount of 13 vol% at T < 500°C, and plagioclase increases from 8 vol% at ~ 500°C to 28 vol% at T > 650°C. It is mostly an andesine, with the anorthite content increasing up-T up to An₄₈; oligoclase compositions (An_{24–30}) are limited to 500–540°C. Significantly higher amounts of zoisite are modelled with respect to Cal0, with a maximum of 8–10 vol% at T < 540°C; its stability field extends up to 620°C (Figure 6b). Calcic amphibole is predicted to be stable in a

narrow temperature range (530–600°C) (Figure 6b) and in relatively high modal amounts (>5 vol%). The garnet stability field and modal amount (up to 10 vol%) are similar to those modelled for Cal0 (Figure 6b). Its composition varies from Alm₅₆Sps₁₁Prp₆Grs₂₇ at 530°C to Alm₆₂Sps₃Prp₁₀Grs₂₅ at T>600°C.

4.2.3 Cal6

The topology of the P/T–X(CO₂) pseudosection modelled for Cal6 (Figure 6c, S2c and S3c) is still very similar to those of Cal0 and Cal3, being dominated by calcite-absent fields. Calcite-bearing fields are limited by the same discontinuous calcite-consuming reactions already discussed for Cal3 (i.e. reactions 30 and 13), but calcite is more abundant (up to 8 vol%). In the temperature range of 500–660°C, less than 10 vol% of muscovite is modelled, and its abundance further decreases at increasing temperature, up to its complete disappearance at 680–700°C (Figure 6c). The disappearance of muscovite leads to the appearance of a small amount (<6 vol%) of K-feldspar. The predicted amount of biotite is similar to that modeled for Cal0 and Cal3, i.e. >20 vol% at 490–700°C. Garnet is modelled in significantly lower amounts, exceeding 1 vol% only at 590–600°C (Figure 6c) and reaching a maximum of 3 vol% at T>680–700°C. Its composition varies from Alm₅₀Sps₁₂Prp₆Grs₃₂ at 590°C to Alm₄₉Sps₆Prp₈Grs₃₇ at 700°C.

Among the calcium-bearing phases, plagioclase is still the most abundant, reaching its maximum amount (>35 vol%) at T>680°C. As for Cal3, it is mostly an andesine, with oligoclase compositions limited to 500–530°C and labradorite compositions at T>660–670°C. The zoisite stability field is significantly enlarged (Figure 6c) with respect to Cal3, and zoisite amounts of more than 10 vol% are predicted for a wide temperature range (400–620°C). Scapolite appears at 580–660 °C for X(CO₂)>0.18 (Figure 6c), in significant modal amounts (up to 20–22 vol%); its stability field is limited toward higher temperature by a decarbonation (although calcite-absent) discontinuous reaction which corresponds to the NKCAS univariant reaction 11 (Mu + Scp + Qz = Pl + Kfs + Zo) (Figure 5). For this bulk composition, calcic amphibole is not predicted to be stable.

4.2.4 Cal9

The topology of the P/T–X(CO₂) pseudosection modelled for Cal9 (Figure 6d, S2d and S3d) differs from those of Cal0, Cal3 and Cal6 because the calcite stability field is significantly enlarged and several discontinuous calcite-consuming reactions thus appear, which are marked by narrow 2 and 3 -variant fields. The first calcite-consuming reaction corresponds to the KCFAS/KCMAS univariant reaction 30 (Cal + Clc/Dph + Mu + Qz = Phl/Ann + Zo) as also discussed for Cal0 to Cal6. At higher temperatures and for X(CO₂)<0.12, two discontinuous KCFAS/KCMAS reactions are responsible for further consumption of calcite: Cal + Phl/Ann + Qz = Di/Hd + Mu (represented by a narrow 3-variant field), and Cal + Phl/Ann + Qz

+ Zo = Grt + Mu (represented by a narrow 2-variant field) (Figure 6d). These reactions, not modelled in the KCFAS/KCMAS projections, are the muscovite-bearing counterparts of the K-feldspar-bearing univariant reactions 27 (Cal + Phl/Ann + Qz = Di/Hd + Kfs) and 32 (Cal + Phl/Ann + Qz + Zo = Grt + Kfs) (Figure 5). The discrepancy between the grids and the pseudosection is due to the choice of not considering the white mica solid solution in the calculation of the grids, which results in a reduced stability field of muscovite with respect to that modelled in the pseudosection. At slightly higher temperature and for $X(\text{CO}_2) = 0.12\text{--}0.14$, two narrow 3-variant fields correspond to the KCAS and KCMAS/KCFAS univariant reactions 6 (Cal + Mu + Qz = Kfs + Zo) and 27 (Cal + Phl/Ann + Qz = Di/Hd + Kfs), respectively (Figures 5 and 6d). At $X(\text{CO}_2) > 0.14$, two relevant discontinuous calcite-consuming reactions appear, which correspond, from lower to higher temperatures to the NCAS and NKAS univariant reactions 2 (Cal + Pl + Zo = Scp) and 10 (Cal + Mu + Pl + Qz = Kfs + Scp). In the calcite-absent fields located above the calcite-out reaction 10, two additional discontinuous decarbonation reactions are modelled, corresponding to the NKAS and NKCMAS univariant reactions 11 (Mu + Scp + Qz = Pl + Kfs + Zo) and 51 (Phl + Qz + Scp = Di + Kfs + Pl + Zo), respectively (Figures 5 and 6d).

The muscovite stability field is further reduced with respect to Cal6, being limited to $T < 600^\circ\text{C}$ at $X(\text{CO}_2) < 0.15$ and to $T < 660^\circ\text{C}$ at $X(\text{CO}_2) > 0.15$ (Figure 6d); its modal amount is mostly in the range 10–15 vol%. At temperature higher than the muscovite breakdown, K-feldspar becomes stable, but does not exceeds 10 vol%. Biotite is the most abundant phyllosilicate: it is predicted to be stable in most of the $P\text{--}T\text{--}X(\text{CO}_2)$ range of interest, with modal amounts higher than 20 vol% at 600–670°C. The chlorite stability field is limited to $T < 470^\circ\text{C}$ (Figure 6d). Small amounts of garnet are predicted to be stable in most of the calcite-absent fields, but modal amounts higher than 1 vol% (and therefore evident) only appear at $T > 640\text{--}650^\circ\text{C}$ (Figure 6d).

Plagioclase/albite is predicted to be stable in the whole $P\text{--}T\text{--}X(\text{CO}_2)$ range of interest, with modal amounts increasing from 18 vol% to more than 35 vol% at increasing temperature; however, in the scapolite bearing fields, its modal abundance decreases to 5–10 vol%. Plagioclase is mostly an andesine, with labradorite compositions limited to $T > 680^\circ\text{C}$. Significant amounts of zoisite are predicted to be stable in both calcite-present and calcite-absent fields, together with plagioclase (Figure 6d). At $X(\text{CO}_2) > 0.15$, scapolite is the most abundant calcium-bearing phase, reaching up to 35 vol%. Differently from Cal0 to Cal6, low amounts (2–8 vol%) of clinopyroxene are predicted to be stable in most of the calcite-absent field (Figure 6d).

4.2.5 Effects of variable amounts of initial calcite on the mineral assemblages

As expected, increasing amounts of calcite in the pelitic protolith enhances the stability of calcium-rich minerals. Plagioclase and zoisite, often present in low amounts in pure metapelites, can increase up to 30 and 15 vol%, respectively, in calcic metapelites. Moreover, other calcium-rich minerals such as amphibole and scapolite can appear at specific P–T–X(CO₂) conditions. The sequence of lithologies that would form during prograde metamorphism of calcareous pelites with 3, 6 and 9 vol% of initial calcite is therefore dramatically different from that of pure metapelites (Figures 6a–d). Calcite would disappear relatively early (i.e. at T<460–470°C) if its initial content in the protolith was low (i.e. for Cal3), but it would remain stable at significantly higher temperatures if its initial content was slightly higher (i.e. for Cal9). If the system evolved along an internally buffered path (see section 5.3), this implies that fluid composition would evolve toward progressively higher X(CO₂) values at increasing temperature.

Two-mica + chlorite + albite -bearing micaschist and white mica(s) + biotite (Mu>Bt) + oligoclase + garnet -bearing micaschist are the dominant metamorphic products of a calcite-free pelitic protolith (Cal0) at progressively increasing temperatures (Figures 6a and 8a). A more complex evolution is instead inferred even just for slightly calcareous pelitic protoliths. For 3 vol% of initial calcite (Cal3), two additional lithologies are predicted to occur at 500–600°C: a two-mica (Mu≈Bt) + oligoclase + zoisite -bearing micaschist at lower temperatures (500–550°C), and a two-mica (Mu≈Bt) + andesine + amphibole + garnet + zoisite -bearing micaschist at higher temperatures (550–600°C) (Figures 6b and 8b). At T>600°C, the metamorphic product of such a slightly calcareous pelite would be a two-mica (Mu≈Bt) + andesine + garnet -bearing micaschist (Figure 8b).

For 6 vol% of initial calcite (Cal6), the metamorphic product developing at 500–650°C is a two-mica + andesine + zoisite ± garnet -bearing micaschist, with biotite always more abundant than muscovite, whereas a labradorite + garnet -bearing biotitic gneiss develops at T>650°C, due to the disappearance of muscovite (Figure 6c and 8c). For 9 vol% of initial calcite (Cal9), a two-mica (Bt>Mu) + andesine + zoisite -bearing micaschist is still the dominant metamorphic product at 500–600°C, but with low amounts of calcite still preserved. At T>600°C, a two-mica (Bt>>Mu) + scapolite + andesine ± zoisite ± garnet micaschist or gneiss is predicted to occur, eventually evolving toward a scapolite + labradorite + garnet biotitic gneiss at T>650°C (Figure 6c and 8c).

4.2.6 Effects of variable Mg/Fe ratio on the mineral assemblages

The influence of variable Mg/Fe ratios was investigated using an additional set of model compositions with a higher MgO/(MgO+FeO) ratio (highMg compositions; Table 2). The effects of a different Mg/Fe ratio are more pronounced for calcite-free and calcite poor pelitic protoliths (i.e. Cal0 and Cal3 bulk compositions) rather than for calcite-rich protoliths (Figure 6). As expected, the most evident

consequence of varying the Mg/Fe ratio is a change in the relative stability of mafic minerals. More specifically, compared to Cal0, Cal3, Cal6 and Cal9 bulk compositions (Figures 6a–d), MgO-enriched bulk compositions (Figures 6e–h) lead to the reduction of the garnet stability field, counterbalanced by the enlargement of chlorite and biotite stability fields. Examining the results more in detail, it emerges that:

- The sequence of prograde assemblages predicted for the MgO-enriched Cal0_highMg bulk composition (Figures 6e and 8e) differs from that predicted for Cal0 because chlorite remains stable up to 570°C, and garnet becomes evident (i.e. exceeds 1 vol%) at T>560–570°C. Moreover, the higher Mg/Fe ratio enhances the stability field of staurolite and kyanite, leading to the development of two-micas, garnet + andesine + staurolite schists at 610–660°C and of two-micas, garnet + andesine + kyanite schists at T>660°C (Figure 6e).
- Compared to Cal3 (Figure 6b), the MgO-enriched Cal3_highMg bulk composition (Figures 6f and 8f) enhances the chlorite and amphibole stability fields at the expense of garnet, whose abundance does not exceed 3 vol%. The sequence of Ca-rich minerals predicted after the final consumption of calcite at T>470°C is the same as that predicted for Cal3 (i.e. zoisite, amphibole and andesine/labradorite; Figure 8f).
- The sequence of prograde assemblages predicted for the MgO-enriched Cal6_highMg (Figures 6g and 8g) and Cal9_highMg bulk compositions (Figures 6h and 8h) is similar to that predicted for Cal6 (Figures 6c and 8c) and Cal9 (Figures 6d and 8d), but with a significant reduction of the garnet stability field, whose abundance never exceeds 1 vol% (i.e. it does not become evident).

4.2.7 Effects of variable amounts of Na₂O on the mineral assemblages

Bulk compositions depleted in Na₂O (lowNa model compositions) are representative of protoliths enriched in illite and depleted in feldspars (i.e. mature pelites) (Figures 3e and 4d). Compared to Cal0, Cal3, Cal6 and Cal9 bulk compositions (Figures 7e–h), Na₂O-depleted bulk compositions (Figures 7a–d) lead to the reduction of the albite/plagioclase stability field, counterbalanced by the enlargement of chlorite and zoisite stability fields. Moreover, for any given P–T–X(CO₂) condition, the amount of muscovite predicted for Na₂O-depleted bulk compositions is always higher (Figures 9a–d) than that predicted for “average” compositions (Figures 9e–h).

Examining the results more in detail, it emerges that:

- During prograde metamorphism, a calcite-free pelitic protolith depleted in Na₂O (Cal0_lowNa) develops mineral assemblages typical of common metapelites, characterized by very low amounts of plagioclase and by the appearance of staurolite and kyanite at 600°C and 650°C, respectively (Figures 7a and 9a).

- For Cal3_lowNa bulk composition, the sequence of prograde lithologies is similar to that predicted for Cal3, but the stability fields of amphibole and chlorite are enlarged (and that of plagioclase is significantly reduced) and muscovite modal amount increases (Figures 7b and 9b). Once that calcite is completely consumed ($<470^{\circ}\text{C}$), CaO is mostly incorporated in zoisite ($<550^{\circ}\text{C}$), amphibole ($530\text{--}640^{\circ}\text{C}$) and labradorite/bytownite ($>640^{\circ}\text{C}$) at progressively increasing temperatures.
- Compared to Cal6, the Na_2O -depleted Cal6_lowNa bulk composition leads to the persistence of chlorite at higher temperatures, to the appearance of amphibole-bearing assemblages at $550\text{--}580^{\circ}\text{C}$ and to an enlargement of the muscovite stability field, which remains stable up to 700°C (Fig. 7c and 9c). Calcite is consumed early in the prograde evolution ($<520^{\circ}\text{C}$) and CaO is mostly incorporated in zoisite (up to 680°C), amphibole ($550\text{--}580^{\circ}\text{C}$) and labradorite/bytownite ($>580^{\circ}\text{C}$). The resulting prograde sequence of assemblages predicted for Cal6_lowNa shows a convergence toward that predicted for Cal3 bulk composition (Figures 7c,f and 9c,f).
- The sequence of prograde assemblages predicted for Cal9_lowNa bulk composition is different from that predicted for Cal9 (Figure 7d), and shows a convergence toward those predicted for Cal6 (Fig. 7g). Calcite remains stable up to 580°C (Figure 7d) but its modal amount is very low ($< 1 \text{ vol}\%$) at $T > 480^{\circ}\text{C}$. Once that calcite is completely consumed, CaO is mostly incorporated in zoisite (up to 700°C) and scapolite ($570\text{--}650^{\circ}\text{C}$), whereas plagioclase (labradorite) becomes relevant only at $T > 650^{\circ}\text{C}$. Similar to what predicted for Cal6, the resulting lithologies are richer in biotite than in muscovite (Figures 7d and 9d).

Bulk compositions enriched in Na_2O (_highNa model compositions) are representative of protoliths enriched in feldspars and depleted in illite (i.e. arkoses or very immature pelites) (Figures 3e and 4d). The effects of Na_2O enrichment are opposite to those of Na_2O depletion: the stability field of albite/plagioclase is enlarged and that of zoisite is reduced compared to Cal0, Cal3, Cal6 and Cal9 bulk compositions, and biotite is the prevalent mica in most lithologies (Figures 7i–l). Furthermore, Na_2O -enriched bulk compositions inhibit the formation of garnet, whose stability field is therefore reduced with respect to “average” compositions.

- The sequence of prograde assemblages predicted for the Na_2O -enriched Cal0_highNa bulk composition is similar to that predicted for Cal0, but with higher amounts of oligoclase (Figures 7i and 9i), that can reach up to 27 vol%.
- Compared to Cal3, the Na_2O -enriched Cal3_highNa bulk composition hampers the formation of amphibole and reduces the stability field and modal amount of garnet (Figures 7j and 9j). After the consumption of calcite at $T < 470^{\circ}\text{C}$, CaO is mostly incorporated in zoisite at lower temperatures and in andesine at $T > 500^{\circ}\text{C}$.

- The sequence of prograde assemblages predicted for Cal6_highNa bulk composition is significantly different from that predicted for Cal6, and shows a convergence toward those predicted for Cal9 (Figures 7k and 9k). Calcite remains stable up to 630°C and for medium grade metamorphic conditions CaO is mostly incorporated in andesine and zoisite. After the final calcite breakdown, scapolite also appears. Similar to what discussed for Cal9, biotite is the dominant mica in all lithologies; moreover, muscovite completely disappears at $T > 600\text{--}630^\circ\text{C}$ (Figures 7k and 9k).
- The sequence of prograde assemblages predicted for the Na_2O -enriched Cal9_high Na bulk composition is similar to that predicted for Cal9, but the calcite stability field is enlarged toward higher T and $X(\text{CO}_2)$ values, the garnet stability field is reduced and clinopyroxene appears at significantly lower temperatures (i.e. at $T > 500^\circ\text{C}$). As a consequence, the scapolite-bearing lithologies can contain small amounts of clinopyroxene ($< 10\text{ vol}\%$) and don't contain garnet (Figures 7l and 9l). CaO is mostly incorporated in andesine, that can exceed 30 vol%, as well as in zoisite (at $T < 570^\circ\text{C}$) or scapolite (at $T > 570^\circ\text{C}$). Muscovite completely disappears at $T > 600\text{--}630^\circ\text{C}$, and biotite is the dominant mica in all the lithologies (Figures 7l and 9l).

5. DISCUSSION

5.1 Predicted vs. observed mineral assemblages

Although the $P/T\text{--}X(\text{CO}_2)$ pseudosections have been calculated for generic, model, bulk compositions, the predicted mineral assemblages can be qualitatively compared with the assemblages observed in the studied samples.

The most common types of calcic metapelites in both the LHS and GHS are represented by Ca-rich plagioclase \pm garnet \pm zoisite -bearing two-micas schists or biotitic gneisses (Types 1 and 2, see section 2.1), with plagioclase anomalously abundant (i.e. often $> 20\text{ vol}\%$) and Ca-richer (i.e. from andesine to labradorite) with respect to the associated metapelites. These assemblages are predicted to occur for a wide range of model compositions, spanning from Cal3 to Cal9). The Na_2O concentration controls the relative abundance of plagioclase, zoisite and garnet (Figure 9): more specifically, zoisite and garnet are more abundant (i.e. Type 1) in Na_2O depleted compositions, whereas plagioclase modal abundance is favored (i.e. Type 2) by Na_2O -enriched compositions. Garnet abundance is also controlled by the Mg/Fe ratio, being favored by MgO-depleted compositions (Figure 8). Moreover, for Na_2O - and MgO- enriched bulk compositions, muscovite is generally predicted to be equally or less abundant than biotite, and it is predicted to completely disappear at $T > 650\text{--}680^\circ\text{C}$ for the calcite-richer model compositions (Figures 8 and 9). The predicted amount of muscovite vs. biotite is in agreement with the observation that samples

from GHS (i.e. equilibrated at higher temperatures) are mostly biotitic gneisses, whereas those from LHS (i.e. equilibrated at lower temperatures) are two-micas schists.

Among the studied samples, those containing scapolite (Types 3 and 4, see section 2.1) are the most intriguing, because they are characterized by a relatively uncommon mineral assemblage. Scapolite occurrence is predicted for calcic metapelites derived from protoliths with relatively high amounts of calcite (Cal9_highMg, Cal9_lowNa, Cal9, Cal9_highNa model compositions) and/or enriched in Na₂O (Cal6_highNa model composition) (Figures 8 and 9). Garnet is predicted to occur in lower amounts with respect to those observed in the studied samples, but its abundance could be eventually influenced by slightly different amounts of MnO in the natural vs. model bulk compositions. Scapolite ± garnet -bearing assemblages are predicted to be stable at 600–680°C, and muscovite is predicted to occur in low amounts only for T<620–650°C, in agreement with the systematic occurrence of the garnet + scapolite-bearing two-micas schists in the lower structural levels of the Lower-GHS (staurolite and kyanite zone: 600–670°C). The stability field of the assemblage scapolite ± garnet + biotite + muscovite is relatively small and limited to X(CO₂) values higher than 0.15 (Figures 8d,h and 9d,h,l). The occurrence of this assemblage in the studied samples is therefore an evidence that the composition of the fluid remained internally buffered during the whole prograde evolution.

The calcic amphibole + garnet -bearing assemblages observed in Type 5 two-micas schists or biotitic gneisses (see section 2.1) are predicted to occur in calcic metapelites derived from protoliths with low amounts of calcite and/or low amounts of Na₂O (i.e. Cal3_highMg, Cal3_lowNa, Cal3 and Cal6_lowNa model compositions), with relatively higher modal amounts of calcic amphibole favored by Na₂O-depleted and MgO-enriched compositions (Figures 8 and 9). The calcic amphibole stability field is mostly limited to T<650°C, in agreement with the systematic occurrence of this lithology in the upper structural levels of the LHS (garnet + staurolite zone: 560–600°C) and in the lower structural levels of the Lower-GHS (staurolite and kyanite zones: 600–670°C).

Overall, there is a good correspondence between the observed and the predicted mineral assemblages, which confirms the validity of the thermodynamic modelling. The comparison between the natural and the modelled assemblages also highlights the internal buffered behavior of the studied calcic metapelites, which is particularly evident for those meta-sediments which originally contained more than 6 vol% of calcite.

5.2 Melt fertility

The results of thermodynamic modelling demonstrate that, at a given temperature, the metamorphic products of calcareous pelites contain significantly less muscovite than pure metapelites. On average, at

650°C, a pure metapelite (Cal0) contains more than 20–25 vol% of muscovite (Figures 8 and 9). This amount decreases to 10–15, 3–7 and 0–3 vol% for increasing amounts (3, 6 and 9 vol%, respectively) of calcite initially present in the protolith (Figures 8 and 9). This is due to the fact that most of the calcium-rich minerals occurring in calcic metapelites (especially plagioclase, zoisite and scapolite) are also rich in Al; their modal increase in progressively more calcic metapelites is thus counterbalanced by a contemporaneous decrease of other Al-bearing minerals, especially muscovite. The result is that calcic metapelites tend to develop muscovite-free, biotite ± K-feldspar -bearing assemblages at temperatures much lower than pure metapelites; the effect is even more pronounced for Na₂O-richer bulk compositions. An important consequence is that assemblages commonly considered as representative of high-grade metamorphic conditions, can be stable at temperatures as low as 610°C in calcic metapelites (Figures 8 and 9).

In common metapelites, muscovite dehydration melting occurs at $T > 700^{\circ}\text{C}$ and, for a given temperature (and pressure), the amount of melt produced through this process varies as a function of muscovite content in the source rock (e.g. Brown, 2013 and references therein). It has been calculated that a pelite containing 10–20 vol% muscovite produces 7–15 vol% of melt through muscovite dehydration melting depending on pressure (e.g. Groppo, Rolfo, & Indares, 2012; Groppo, Rolfo, & Mosca, 2013; Spear, Kohn, & Cheney, 1999). Containing minor amounts of muscovite, calcic metapelites are undoubtedly less fertile than common metapelites, at least at $T < 800^{\circ}\text{C}$ (i.e. at temperatures lower than those required for significant biotite dehydration melting). For initial calcite content of 6–9 vol%, muscovite dehydration melting can even not occur, because muscovite disappears well below the solidus of the system, and biotite dehydration melting would mark therefore the first appearance of melt. Although a deeper investigation of partial melting processes in calcic metapelites is well beyond the aim of this paper, it can be suggested that their behavior could be more similar to that of meta-greywackes (e.g. Patiño Douce, & Beard, 1996; Vielzeuf, & Montel, 1994; Vielzeuf, & Schmidt, 2001) rather than to that of pure metapelites (e.g. Johnson, White, & Powell, 2008; Spear et al., 1999; White et al., 2001, 2007). More specifically, it is likely that up to $\sim 800^{\circ}\text{C}$ the melt productivity of calcic metapelites remains low, and that melt production occurs gradationally (i.e. in a wide temperature range and not by steps), because it is mostly controlled by continuous biotite dehydration melting reactions.

5.3 Fluid evolution and decarbonation processes

The results of our thermodynamic modelling allow us to investigate how CO₂ is released from calcareous sediments during prograde metamorphism (i.e. through which reactions and at which P–T conditions), as well as the maximum amounts of CO₂ released as a function of the initial calcite content in the protolith.

An internally buffered behavior is considered for the discussion, following Greenwood (1975) and Baker, Holland, & Powell (1991) and in agreement with what suggested by the mineral assemblages observed in the studied samples (see Section 5.1). Quantitative calculation of a buffering path requires exact knowledge of the initial composition of the fluid in the protolith (e.g. Elmer et al., 2006; Kuhn et al., 2005). Unlike for the calculation of $P/T-X(\text{CO}_2)$ pseudosections, where the fluid is considered as a saturated phase (i.e. the amounts of H_2O and CO_2 are not fixed by the user), the amounts of H_2O and CO_2 in the bulk rock must be given in the calculation of the paths. This implies adding a certain proportion of fluid to the mineral assemblage at the starting point of the paths. The choice of the amount of fluid to be added and of its equilibrium composition could seem subjective, as it is. However, it is functional to the general discussion (see also Elmer et al., 2006) and it can be considered reliable as far as the results of the modeling are compatible with the final metamorphic assemblages observed in the studied samples.

We added an initial mole proportion of fluid of 0.05 (5 mol%), which approximately corresponds to 4 vol% of fluid at 400°C, a value that is fully consistent with the experimentally determined porosity (1–16%) of metapelites at low pressure ($P < 5$ kbar, i.e. at the starting conditions) (Bruijn, & Almqvist, 2014). The initial equilibrium fluid composition was assumed to be $X(\text{CO}_2) = 0.00694$. The fluid-rock buffering paths have been quantitatively calculated following the constant porosity model of Elmer et al. (2006). According to this model, the fluid is allowed to accumulate within the rock until it reaches a specified threshold; each time this threshold is exceeded, fluid loss occurs through a stepwise process. Starting from the initial fluid mole proportion of 0.05, we have fixed the threshold at 0.06; this implies that when the fluid proportion reaches this value, it is reduced to 0.05. Fixing a different threshold would result in different buffering paths; to understand the influence of the assumed threshold on the resulting buffering paths we have considered the two extreme cases of a completely closed system (i.e. no fluid loss is allowed) and of a completely open system (i.e. all the fluid that is produced is immediately lost). Whatever was the real behavior of the system, the buffering path should be comprised in between these two extremes. The calculated fluid-rock buffering paths are reported in Figures 6–7; Figures 8–11 summarize the variation of mineral assemblages and the CO_2 -producing reactions encountered along these paths for each model composition.

For very minor amounts of initial calcite in the protolith (1–5 vol%: Cal3 group), calcite is consumed relatively early in the metamorphic evolution, mostly in the temperature range 460–470°C (Figures 10 a,d and 11a,d,g). Most of CO_2 is released through the discontinuous dehydration and decarbonation reactions 30 ($\text{Cal} + \text{Clc/Dph} + \text{Mu} + \text{Qz} = \text{Phl/Ann} + \text{Zo}$), i.e. in a very narrow P – T interval. The buffering capacity of these rocks is low and the fluid produced is extremely enriched in H_2O , with $X(\text{CO}_2)$ values < 0.05 (Figures 8b,f, 9b,f,j).

For slightly higher amounts of calcite in the pelitic protolith (5–8 vol%: Cal6 group), the decarbonation behavior of calcareous sediments can change significantly, depending on the bulk composition, and especially on its Na₂O content. In most cases, calcareous sediments with 5–8 vol% of original calcite experience decarbonation processes similar to those described for Cal3, with calcite completely consumed at T<550°C and the release of a H₂O-rich fluid (X(CO₂)<0.10) (Figures 10b,e and 11b,e). However, for Na₂O-enriched bulk compositions (Cal6_highNa), an initial amount of calcite of 5–6 vol% in the protolith is sufficient to increase the calcite stability field up to ~ 610°C (Figure 9k). The discontinuous reactions 30 still represents the first important stage of CO₂ production (Figure 11h), but it does not cause the complete consumption of calcite. If the system remains internally buffered, it evolves along the calcite-bearing fields, up to the discontinuous decarbonation and dehydration reactions 27* (Cal + Bt + Qz = Cpx + Mu) and 27 (Cal + Bt + Qz = Cpx + Kfs), which are responsible for the appearance of very low amounts (< 0.5 vol%) of clinopyroxene in the equilibrium assemblage. The final consumption of calcite occurs at about 610°C through the discontinuous dehydration reaction 2 (Cal + Pl + Zo = Scp), which produces scapolite (Figure 11h). A small amount of CO₂ is still released at higher temperatures through the scapolite-consuming discontinuous reaction 51 (Bt + Qz + Scp = Cpx + Kfs + Pl + Zo) until the final disappearance of scapolite which occurs at about 620°C. At the end of the decarbonation history, the fluid is relatively enriched in CO₂ (X(CO₂) = 0.15) (Figures 9k and 11h).

For calcareous sediments with 8–11 vol% of initial calcite (Cal9), the decarbonation history varies as a function of the Na₂O content. In Na₂O-depleted bulk compositions (Cal9_lowNa), the discontinuous reaction 30 represents the first important stage of CO₂ production at T<470°C (Figure 11c); at higher temperatures, decarbonation occurs through discontinuous reactions involving ankerite (not modeled in detail in this study). After the final consumption of carbonates at T=570°C, further decarbonation still occurs through scapolite-consuming continuous reactions, until the final disappearance of scapolite, which occurs at about 670°C through the discontinuous decarbonation and dehydration reaction 11 (Mu + Qz + Scp = Kfs + Pl + Zo) (Figure 11c). For intermediate amounts of Na₂O in the bulk composition (Cal9 and Cal9_highMg), the calcite stability field is enlarged up to ~ 610°C; if the system remains internally buffered, after the first important stage of CO₂ production through reaction 30, it evolves along the calcite-bearing fields, and calcite is completely consumed through the discontinuous decarbonation and dehydration reaction 6 (Cal + Mu + Qz = Kfs + Zo) and the discontinuous dehydration reaction 2 (Cal + Pl + Zo = Scp) (Figures 10c,f). Further decarbonation, however, still occurs through the two discontinuous scapolite-consuming reactions 11 and 51, in the temperature range of 610–690°C (Figures 10c,f). In Na₂O-enriched bulk compositions (Cal9_highNa), the fluid evolution is similar to that described for Cal6_highNa (i.e. decarbonation occurs through reactions 30, 27*, 27, and 2) until the final consumption of calcite. At

$T > 610^{\circ}\text{C}$, however, the system evolves along the scapolite-bearing fields, with further decarbonation mostly occurring through continuous reactions (Figure 11i). In all cases, the final fluid released from calcareous sediments with 8–11 vol% of initial calcite (Cal9) is relatively enriched in CO_2 (i.e. $X(\text{CO}_2) = 0.25, 0.27$ and 0.31 for increasing Na_2O in the bulk) (Figures 9d,h,l).

The CO_2 productivity of calcic metapelites is controlled by the initial proportion of calcite in the protolith. If calcite is completely consumed during prograde metamorphism, as it is predicted to occur in most LHS and GHS lithologies, the CO_2 productivity ranges between approximately 1.3 and 2.5 wt% for initial calcite modal proportions of 3 to 6 vol%, and reaches 4 wt% for initial calcite contents of 9–10 vol%. [CO_2 productivities have been calculated according to the following reasoning: 1 vol % of calcite corresponds to 1 cm^3 of calcite within 100 cm^3 of rock; calcite has a density of 2.7 g/cm^3 and an average density of 2.8 g/cm^3 is assumed for the hosting rock; this means that 1 vol% of calcite equals to $2.7 \text{ g} / 280 \text{ g} = 0.96 \text{ wt\%}$ of calcite. The molar weights of CaO and CO_2 are 56 g/mol and 44 g/mol , respectively; 1 mole of calcite (CaCO_3) thus weights 100 g (i.e. 1 g of calcite consists of 0.56 g of CaO and 0.44 g of CO_2). To obtain the amount of CO_2 released by 1 vol% of calcite, we thus need to multiply $0.96 \times 0.44 = 0.42 \text{ wt\%}$ of CO_2]. The results of thermodynamic modelling demonstrate that, when the initial amount of calcite in the protolith is low (3–6 vol%), this is completely consumed in a single, step-like, metamorphic stage at low temperatures (mostly in the range $460\text{--}470^{\circ}\text{C}$). However, for higher initial proportions of calcite in the protolith (6–9 vol%), calcite remains stable during most of the prograde metamorphic evolution and it is eventually completely consumed only at $T > 610^{\circ}\text{C}$; furthermore, in most cases, the final disappearance of calcite does not correspond to the end of decarbonation processes, which can proceed until the final consumption of scapolite at $T > 650^{\circ}\text{C}$. In this second case, decarbonation is thus a long-lasting continuous process, rather than a step-like discontinuous process.

A final important consequence is that although CO_2 productivity of calcareous sediments containing 3–6 vol% of initial calcite is relatively low, that of sediments originally containing up to 10 vol% of calcite starts to be relevant, being of the same order of magnitude than that of meta-sediments originally containing much more calcite. The CO_2 productivity of calc-silicate rocks deriving from marls originally containing 30–40 vol% of calcite was, in fact, estimated to be in the range 4.5–5.5 wt% (Groppo et al., 2017), calcite being only partially consumed during prograde metamorphism. Therefore, we suggest that calcareous pelites should not be ignored as likely CO_2 -source rocks when computing the global budget of CO_2 emissions related to orogenic metamorphism.

ACKNOWLEDGEMENTS

The studied samples were collected during fifteen field campaigns in central-eastern Nepal, which were mostly funded by the Italian Ministry of University and Research (PRIN2006, Project n°: 2006040882_003; PRIN2010–2011, Project n°: 2010PMKZX7; PRIN2015, Project n°: 015EC9PJ5) and by the Compagnia di San Paolo and University of Torino (Junior PI Grant, Project n°: TO_Call1_2012_0068).

Laboratory work was funded by the Italian Ministry of University and Research (PRIN 2017, Project n°: 2017LMNLAW) and by the University of Torino (Ricerca Locale, ex-60% 2018 funds: ROLF_RILO_18_01).

We thank P. Pitra and J. Diener for their constructive comments which significantly improved this work. R. White is thanked for editorial handling.

REFERENCES

- Ague, J. J. (1991). Evidence for major mass transfer and volume change during regional metamorphism of pelites. *Geology*, 19, 855–858.
- Baker, J., Holland, T. J. B., & Powell, R. (1991). Isograds in internally buffered systems without solid solutions: principles and examples. *Contributions to Mineralogy and Petrology*, 106, 170–182.
- Brown, M. (2013). Granite: from genesis to emplacement. *Geological Society of America Bulletin*, 125, 1079–1113.
- Bruijn, R.H.C., & Almqvist, B.S.G. (2014). The role of stress on chemical compaction of illiteshale powder. In: Faulkner, D.R., Mariani, E., & Mecklenburgh, J. (eds) *Rock Deformation from Field, Experiments and Theory: A Volume in Honour of Ernie Rutter*. Geological Society, London, Special Publications, 409, SP409.3.
- Bucher, K. & Grapes, R. (2011). *Petrogenesis of Metamorphic Rocks*, 8th edition. Springer. 428 pp.
- Carmichael, R. S. (1989). *Practical Handbook of Physical Properties of Rocks and Minerals*. CRC Press. Boca Raton. 7 pp.
- Condie, K. C. (1993). Chemical composition and evolution of the upper continental crust: Contrasting results from surface samples and shales. *Chemical Geology*, 104, 1–37.
- Connolly, J. A. D. (1990). Multivariable phase diagrams: an algorithm based on generalized thermodynamics. *American Journal of Science*, 290, 666–718.
- Connolly, J. A. D. (2009). The geodynamic equation of state: what and how. *Geochemistry, Geophysics, Geosystems*, 10, Q10014.
- Dyck, B., St-Onge, M., Searle, M. P., Rayner, N., Waters, D., & Weller, O. M. (2018). Protolith lithostratigraphy of the Greater Himalayan Series in Langtang, Nepal: implications for the architecture of the northern Indian margin. In: Treloar, P. J. & Searle, M. P. (eds): *Himalayan Tectonics: A Modern Synthesis*. Geological Society of London, Special Publications, 483, 281–304.
- Elmer, F. L., White, R. W., & Powell, R. (2006). Devolatilization of metabasic rocks during greenschist–amphibolite facies metamorphism. *Journal of metamorphic Geology*, 24, 497–513.
- Ferry, J. M. (1976). Metamorphism of calcareous sediments in the Waterville–Vassalboro area, south–central Maine: mineral reactions and graphical analysis. *American Journal of Science*, 276, 841–882.
- Ferry, J. M. (1983a). On the control of temperature, fluid composition and reaction progress during metamorphism. *American Journal of Science*, 283A, 201–232.
- Ferry, J. M. (1983b). Regional metamorphism of the Vassalboro Formation, south–central Maine, USA: a case study of the role of a fluid in metamorphic petrogenesis. *Journal of the Geological Society of London*, 140, 551–576.

- Ferry, J. M. (1992). Regional metamorphism of the Waits River Formation, eastern Vermont: delineation of a new type of giant metamorphic hydrothermal system. *Journal of Petrology*, 33, 45–94.
- Godard, G. (2009). Two orogenic cycles in eclogite-facies gneisses of the Southern Armorican Massif (France). *European Journal of Mineralogy*, 21, 1173–1190.
- Goscombe, B., Gray, D., & Foster D.A. (2018). Metamorphic response to collision in the Central Himalayan Orogen. *Gondwana Research*, 57, 191–265.
- Green, E.C.R., White, R.W., Diener, J.F.A., Powell, R., Holland, T.J.B., & Palin R.M. (2016). Activity–composition relations for the calculation of partial melting equilibria in metabasic rocks. *Journal of metamorphic Geology*, 34, 845–869.
- Greenwood, H. J. (1975). Buffering of pore fluids by metamorphic reactions. *American Journal of Science*, 275, 573–593.
- Gromet, L. P., Dymek, R., Haskin, L. A., & Korotev, R. L. (1984). The “North American Shale Composite”: Its compilation, major and trace element characteristics. *Geochimica et Cosmochimica Acta*, 48, 2469–2482.
- Groppo, C., Rolfo, F. & Indares, A. (2012). Partial melting in the Higher Himalayan Crystallines of Eastern Nepal: the effect of decompression and implications for the “channel flow” model. *Journal of Petrology*, 53, 1057–1088.
- Groppo, C., Rolfo, F., & Lombardo, B. (2009). P–T evolution across the Main Central Thrust Zone (Eastern Nepal): hidden discontinuities revealed by petrology. *Journal of Petrology*, 50, 1149–1180.
- Groppo, C., Rolfo, F., & Mosca, P. (2013b). The cordierite-bearing anatectic rocks of the Higher Himalayan Crystallines (eastern Nepal): low-pressure anatexis, melt-productivity, melt loss and the preservation of cordierite. *Journal of Metamorphic Geology*, 31, 187–204.
- Groppo, C., Rolfo, F., Castelli, D. & Mosca, P. (2017). Metamorphic CO₂ production in collisional orogens: petrologic constraints from phase diagram modeling of Himalayan, scapolite-bearing, calc-silicate rocks in the NKC(F)MAS(T)HC system. *Journal of Petrology*, 58, 53–83.
- Groppo, C., Rolfo, F., Castelli, D., & Connolly, J.A.D. (2013a). Metamorphic CO₂ production from calc-silicate rocks via garnet-forming reactions in the CFAS–H₂O–CO₂ system. *Contribution to Mineralogy and Petrology*, 166, 1655–1675.
- Hewitt, D. A. (1973). The metamorphism of micaceous limestones from South–Central Connecticut. *American Journal of Science*, 273A, 444–469.
- Hodges, K. (2000). Tectonics of Himalaya and southern Tibet from two perspectives. *Geological Society of American Bulletin*, 112, 324–350.

- Hofer, G., Wagreich, M., & Neuhuber, S. (2013). Geochemistry of fine-grained sediments of the upper Cretaceous to Paleogene Gosau Group (Austria, Slovakia): Implications for paleoenvironmental and provenance studies. *Geosciences Frontiers*, 4, 449–468.
- Holland, T. J. B., & Powell, R. (1998). An internally consistent thermodynamic data set for phases of petrologic interest. *Journal of metamorphic Geology*, 16, 309–343.
- Holland, T. J. B., & Powell, R. (2011). An improved and extended internally consistent thermodynamic dataset for phases of petrological interest, involving a new equation of state for solids. *Journal of metamorphic Geology*, 29, 333–383.
- Johnson, T.E., White, R.W., Powell R. (2008). Partial melting of metagreywacke: a calculated mineral equilibria study. *Journal of metamorphic Geology*, 26, 837–853.
- Kohn, M. J. (2014). Himalayan metamorphism and its tectonic implications. *Annual Review of Earth and Planetary Science Letters*, 42, 381–419.
- Kuhn, B. K., Reusser, E., Powell, R., & Günther, D. (2005). Metamorphic evolution of calc-schists in the Central Alps, Switzerland. *Schweizerische Mineralogische und Petrographische Mitteilungen*, 85, 175–190.
- Massonne, H. J. (2010). Phase relations and dehydration behaviour of calcareous sediments at very-low to low grade metamorphic conditions. *Periodico di Mineralogia*, 79, 21–43.
- McLennan, S.M., Hemming, S., McDaniel, D.K., & Hanson, G.N. (1993). Geochemical approaches to sedimentation, provenance, and tectonics. *Geological Society of America, Special Paper*, 284, 21–40.
- Menard, T., & Spear, F. S. (1993). Metamorphism of Calcic Pelitic Schists, Strafford Dome, Vermont: Compositional Zoning and Reaction History. *Journal of Petrology*, 34, 977–1005.
- Mosca, P., Groppo, C., & Rolfo F. (2012). Structural and metamorphic features of the Main Central Thrust Zone and its contiguous domains in the eastern Nepalese Himalaya. *Journal of the Virtual Explorer*, 41, paper 2.
- Nabelek, P.I., & Chen, Y. (2014). The initial garnet-in reaction involving siderite–rhodochrosite, garnet re-equilibration and P–T–t paths of graphitic schists in the Black Hills orogen, South Dakota, USA. *Journal of metamorphic Geology*, 32, 133–150.
- Newton, R. C., Charlu, T. V., & Kleppa, O. J. (1980). Thermochemistry of the high structural state plagioclases. *Geochimica et Cosmochimica Acta*, 44, 933–941.
- Patiño Douce, A.E., & Beard, J.S. (1996). Effects of P, f(O₂) and Mg/Fe ratio on dehydration melting of model metagreywackes. *Journal of Petrology*, 37, 999–1024.
- Pearson, O.N., & DeCelles, P.G. (2005). Structural geology and regional tectonic significance of the Ramgarh Thrust, Himalayan fold-thrust belt of Nepal. *Tectonics*, 24, TC4008.

- Pettijohn, F. J. (1957). *Sedimentary Rocks* (2nd ed.). New York: Harper & Brothers. 718 pp.
- Rapa, G., Groppo, C., Mosca, P., & Rolfo, F. (2016). Petrological constraints on the tectonic setting of the Kathmandu Nappe in the Langtang–Gosainkund–Helambu regions, central Nepal Himalaya. *Journal of metamorphic Geology*, 34, 999–1023.
- Rapa, G., Groppo, C., Rolfo, F., Petrelli, M., Mosca, P., & Perugini, D. (2017). Titanite-bearing calc-silicate rocks constrain timing, duration and magnitude of metamorphic CO₂ degassing in the Himalayan belt. *Lithos*, 292–293, 364–378.
- Rapa, G., Mosca, P., Groppo, C., & Rolfo, F. (2018). Detection of tectonometamorphic discontinuities within the Himalayan orogen: structural and petrological constraints from the Rasuwa district, central Nepal Himalaya. *Journal of Asian Earth Sciences*, 158, 266–286.
- Rolfo, F., Groppo, C., & Mosca, P. (2015). Petrological constraints of the “Channel Flow” model in eastern Nepal. In: Mukherjee, S., Carosi, R., van der Beek, P. A., Mukherjee, B. K., & Robinson, D. M. (eds.): *Tectonics of the Himalaya. Geological Society of London, Special Publication*, 412, 177–197.
- Rolfo, F., Groppo, C., & Mosca, P. (2017). Metamorphic CO₂ production in calc-silicate rocks from the eastern Himalaya. *Italian Journal of Geosciences*, 136, 28–38.
- Shaw, D. M. (1956). Geochemistry of pelitic rocks. III. Major elements and general geochemistry. *Geological Society of American Bulletin*, 67, 919–934.
- Spear, F. S., Kohn, M. J., & Cheney, J. T. (1999). P–T paths from anatectic pelites. *Contributions to Mineralogy and Petrology*, 134, 17–32.
- Taylor, S. R., & McLennan, S. M. (1985). *The Continental Crust: its Composition and Evolution*. Blackwell, Oxford. 312 pp.
- Thompson, A. B., & Hovis, G. L. (1979). Entropy of mixing in sanidine. *American Mineralogist*, 64, 57–65.
- Thompson, A. B. (1975). Mineral Reactions in a Calc-Mica Schist from Gassetts, Vermont, U.S.A. *Contribution to Mineralogy and Petrology*, 53, 105–127.
- Upreti, B. N. (1999). An overview of the stratigraphy and tectonics of the Nepal Himalaya. *Journal of Asian Earth Sciences*, 17, 577–606.
- Vance, D., & Holland, T. J. B. (1993). A detailed isotopic and petrological study of a single garnet from the Gassetts Schist, Vermont. *Contribution to Mineralogy and Petrology*, 114, 101–118.
- Vielzeuf, D., & Montel, J.M. (1994). Partial melting of metagreywackes. Part I. Fluid-absent experiments and phase relationships. *Contributions to Mineralogy and Petrology*, 117, 375–393.
- Vielzeuf, D., & Schmidt, M.W. (2001). Melting relations in hydrous systems revisited: application to metapelites, metagreywackes and metabasalts. *Contributions to Mineralogy and Petrology*, 141, 251–267.

- White, R. W., Powell, R., & Holland, T. J. B. (2001). Calculation of partial melting equilibria in the system $\text{Na}_2\text{O}-\text{CaO}-\text{K}_2\text{O}-\text{FeO}-\text{MgO}-\text{Al}_2\text{O}_3-\text{SiO}_2-\text{H}_2\text{O}$ (NCKFMASH). *Journal of metamorphic Geology*, 19, 139–153.
- White, R. W., Powell, R., & Holland, T. J. B. (2007). Progress relating to calculation of partial melting equilibria for metapelites. *Journal of metamorphic Geology*, 25, 511–527.
- White, R. W., Powell, R., & Johnson, T. E. (2014b). The effect of Mn on mineral stability in metapelites revisited: new a–x relations for manganese-bearing minerals. *Journal of metamorphic Geology*, 32, 809–828.
- White, R. W., Powell, R., Holland, T. J. B., Johnson, T. E., & Green, E. C. R. (2014a). New mineral activity–composition relations for thermodynamic calculations in metapelitic systems. *Journal of metamorphic Geology*, 32, 261–286.
- Whitney, D. L., & Evans B. W. (2010). Abbreviations for names of rock-forming minerals. *American Mineralogist*, 95, 185–187.
- Worley, B., & Powell, R. (1998). Singularities in NCKFMASH ($\text{Na}_2\text{O}-\text{CaO}-\text{K}_2\text{O}-\text{FeO}-\text{MgO}-\text{Al}_2\text{O}_3-\text{SiO}_2-\text{H}_2\text{O}$). *Journal of metamorphic Geology*, 16, 169–188.
- Yardley, B. Y. (1977). Relationships between the chemical and modal compositions of metapelites from Connemara, Ireland. *Lithos*, 10, 235–242.
- Zen, E. (1981). A study of progressive regional metamorphism of pelitic schists from the Taconic allochthon of southwestern Massachusetts and its bearing on the geologic history of the area. US Geological Survey Professional Paper 1113, US Government Printing Office, Washington DC. 128 pp.

SUPPORTING INFORMATION

Additional supporting information may be found online in the Supporting Information section at the end of the article.

Figure S1 – Samples location.

Figure S2 – P/T–X(CO_2) pseudosections calculated for the model bulk compositions Cal0 (a), Cal3 (b), Cal6 (c) and Cal9 (d) highlighting the phase-in lines.

Figure S3 – P/T–X(CO_2) pseudosections calculated for the model bulk compositions Cal0 (a), Cal3 (b), Cal6 (c) and Cal9 (d) and modal amounts (vol%) of the main minerals.

Figure S4 – P/T–X(CO_2) pseudosections calculated for the model bulk compositions Cal0_highMg (a), Cal3_highMg (b), Cal6_highMg (c) and Cal9_highMg (d) and modal amounts (vol%) of the main minerals.

Figure S5 – P/T–X(CO₂) pseudosections calculated for the model bulk compositions Cal0_lowNa (a), Cal3_lowNa (b), Cal6_lowNa (c) and Cal9_lowNa (d) and modal amounts (vol%) of the main minerals.

Figure S6 – P/T–X(CO₂) pseudosections calculated for the model bulk compositions Cal0_highNa (a), Cal3_highNa (b), Cal6_highNa (c) and Cal9_highNa (d) and modal amounts (vol%) of the main minerals.

Table S1 – Petrographic features and location of a representative selection of calcic metapelites from the LHS and GHS of Nepal Himalaya.

Figure captions

Figure 1 – Representative microstructures and mineral assemblages of Type 1 (a–g) and Type 2 (h) calcic metapelites from the Lesser Himalayan Sequence (LHS) and Greater Himalayan Sequence (GHS) of Nepal Himalaya. (a) Garnet + zoisite plagioclase –bearing two micas-schist. Garnet and zoisite occur as pluri-mm porphyroblasts, whereas plagioclase is dispersed in the matrix and replaces zoisite (Plane Polarized Light, PPL). The inset shows a detail of zoisite partially replaced by plagioclase (Crossed Polarized Light, XPL). (b) Garnet + plagioclase two micas-schist; garnet and plagioclase are respectively porphyroblasts syn- and post-kinematic with respect to the main foliation (PPL, XPL). (c) Garnet + plagioclase + clinozoisite biotitic schist: garnet poikiloblasts include quartz, plagioclase and clinozoisite (PPL, XPL). (d) Garnet + plagioclase –bearing biotitic gneissic micaschist: garnet porphyroblasts are syn-kinematic with respect to the main foliation, whereas plagioclase overgrows it (PPL). The inset shows a detail of a garnet porphyroblast with relict calcite inclusions (XPL). (e) Plagioclase+ garnet –bearing biotitic gneiss: note the high relief of plagioclase, which is interstitial between quartz and biotite (PPL; inset. XPL). (f) Zoisite + plagioclase + garnet –bearing biotitic gneiss: zoisite and plagioclase are coarse-grained and mostly aligned to the main foliation (PPL, XPL). (g) Plagioclase + garnet –bearing biotitic schist: plagioclase statically overgrows the main foliation defined by biotite (PPL, XPL). (h) Plagioclase-bearing biotitic gneissic micaschist: note the high relief of plagioclase, which is dispersed in the matrix (PPL, XPL).

Figure 2 – Representative microstructures and mineral assemblages of Type 3 (a–d), type 4 (e,f) and Type 5 (g,h) calcic metapelites from LHS and GHS of Nepal Himalaya. (a) Garnet + scapolite –bearing two-micas schist: note that biotite is significantly more abundant than muscovite. Scapolite is mostly concentrated in lens-like domains (PPL, XPL). (b) Garnet + scapolite –bearing biotitic schist: garnet porphyroblasts have a skeletal habit and scapolite is concentrated in millimetric lenses (PPL, XPL). (c) Garnet + scapolite –bearing two-micas schist, with biotite less abundant than biotite. Scapolite is mostly concentrated in lens-like domains (PPL, XPL). (d) Garnet + scapolite –bearing biotitic gneiss: note the skeletal habit of garnet and the fine-grained scapolite dispersed in the matrix (PPL, XPL). (e) Plagioclase + scapolite –bearing biotitic gneiss: plagioclase occurs in pluri-mm poikiloblasts including quartz, whereas scapolite is associated with the biotite layers (PPL, XPL). (f) Scapolite + plagioclase biotitic gneiss: both plagioclase and scapolite are granoblastic (PPL, XPL). (g) Two-micas, garnet + amphibole –bearing phylladic micaschist: garnet porphyroblasts include an internal rotated foliation, whereas the colorless amphibole porphyroblasts statically overgrow the main foliation (PPL, XPL). (h) Garnet + amphibole –bearing biotitic gneiss: garnet has a skeletal habit and amphibole is pale-green (PPL, XPL).

Figure 3 – Measured and model bulk rock compositions for a wide range of meta-sediments discussed in this paper, plotted in the CaO–K₂O– (FeO+MgO) (a), CaO–Al₂O₃– (FeO+MgO) (b), CaO–Na₂O–(FeO+MgO) (c), CaO–MgO–FeO (d) compositional diagrams (mol%), as well as in the phyllosilicate-calcite-(quartz+feldspars) ternary diagram (e) (vol%). The colored diamonds refer to Himalayan meta-sediments derived from calcareous pelites (orange to dark red), marls (dark grey) and impure limestones (light grey); the yellow asterisks refer to Himalayan meta-sediments derived from pelites *sensu stricto*. The numbered squares are average pelite or metapelite compositions from the literature (see the legend), whereas the circles with a colored contour represent the model bulk compositions used for thermodynamic modeling. Vol% of calcite reported in (a), (b), (c) and (d) (grey dotted lines) refer to the reconstructed approximate protolith's mineral compositions (see text for further explanation) and are coherent with those reported in (e) and in Figure 4.

Figure 4 – Approximate protolith's mineral composition calculated basing on the measured bulk compositions (same data as in Figure 3) for: (a) Himalayan calcic metapelites, calc-silicate rocks and impure marbles; (b) Himalayan metapelite *sensu stricto*; (c) average pelites and metapelites from the literature, as reported in Fig. 3 and Table 1d; (d) model bulk compositions used in this study.

Figure 5 – P/T–X(CO₂) projections calculated along a P/T gradient typical of collisional orogenic settings, showing invariant and univariant equilibria for the NKCMAS–H₂O–CO₂ and NKCFAS–H₂O–CO₂ sub-systems. The large black circles are invariant points; the small, white circles are singular points.

Figure 6 – Results of phase equilibria modeling calculation for Cal0 (a,e), Cal3 (b,f), Cal6 (c,g) and Cal9 (d,h) model bulk compositions with variable MgO concentrations: (a–d) “average”-MgO compositions; (e–h) MgO-enriched compositions. Rock types are defined according to the main mineral assemblages; phase abundances lower than 1 vol% are considered irrelevant for the definition of the main lithologies. Distinction among schists and gneisses is based on the modal amount of phyllosilicates (i.e. >25 vol% for schists, <25vol% for gneisses). Numbers from 1 to 5 in the legend refer to the main lithological types recognized in the studied calcic metapelites from the LHS and GHS of Nepal Himalaya (see Figures 1 and 2). The insets in each diagram refer to the approximate protolith's mineral composition as reported in Figure 4. The grey arrows are the hypothetical, yet quantitative, P/T–X(CO₂) paths followed by each model composition in the hypothesis that the system remained internal buffered along the whole prograde evolution: continuous line = fluid-rock buffering path according to a constant porosity model (i.e. the fluid

is allowed to accumulate within the rock until it reaches a specified threshold, after which fluid loss occurs); dotted line = fluid-rock buffering path in a completely closed system (i.e. no fluid loss is allowed); dashed line = fluid-rock buffering path in a completely open system (i.e. all the fluid that is produced is immediately lost). The grey dashed field in each diagram is the stability field of ankerite-dolomite and is not considered in this study. Details on field assemblages, mineral abundances and plagioclase composition are given in Figures S2–S4.

Figure 7 – Results of phase equilibria modeling calculation for Cal0 (a,e,i), Cal3 (b,g,j), Cal6 (c,g,k) and Cal9 (d,h,l) model bulk compositions with variable Na₂O concentrations: (a–d) Na₂O-depleted compositions; (e–h) average-Na₂O compositions; (i–l) Na₂O-enriched compositions. All the other details are as in Figure 6. Details on field assemblages, mineral abundances and plagioclase composition are given in Figures S2, S5 and S6.

Figure 8 - Modebox plots of changes in calculated mineral proportions and fluid composition (X(CO₂), dotted black lines) during prograde metamorphism along the internal buffered P/T–X(CO₂) paths reported in Figure 6: (a,e) Cal0, (b,f) Cal3, (c,g) Cal6, (d,h) Cal9 model bulk compositions with variable MgO concentrations. Plagioclase is reported in blue, with progressively darker tones for increasing anorthite contents (mainly from oligoclase to labradorite compositions, as reported in each diagram). Types 1 to 5 refer to the main lithologies recognized in the studied calcic metapelites from the LHS and GHS of Nepal Himalaya (see Figures 1 and 2).

Figure 9 – Modebox plots of changes in calculated mineral proportions and fluid composition (X(CO₂), dotted black line) during prograde metamorphism along the internal buffered P/T–X(CO₂) paths reported in Figure 7: (a,e,i) Cal0, (b,f,j) Cal3, (c,g,k) Cal6, (d,h,l) Cal9 model bulk compositions with variable Na₂O concentrations. All the other details are as in Figure 8.

Figure 10 – Results of phase equilibria modeling calculation for Cal3 (a,d), Cal6 (b,e) and Cal9 (c,f) model bulk compositions with variable MgO concentrations (same P/T–X(CO₂) pseudosections as in Figure 6) showing the main decarbonation reactions relevant for calcic metapelites (reactions labels and colors as in Figure 5). Note that the univariant curves overlap the (narrow) di- and tri-variant fields of the underlying pseudosections. The dashed arrows are the same P/T–X(CO₂) paths as in Figure 6 (i.e. fluid-rock buffering paths according to a constant porosity model).

Figure 11 – Results of phase equilibria modeling for Cal3 (a,d,g), Cal6 (b,e,h) and Cal9 (c,f,i) model bulk compositions with variable Na₂O concentrations (same P/T–X(CO₂) pseudosections as in Figure 7) showing the main decarbonation reactions relevant for calcic metapelites (reactions labels and colors as in Figure 5). The dashed arrows are the same P/T–X(CO₂) paths as in Figure 7 (i.e. fluid-rock buffering paths according to a constant porosity model).

Table 1a. Bulk compositions (mol%) of meta-sediments ranging from calcic metapelites to calc-silicate rocks

| Calcic metapelites (protolith = calcareous pelites) | | | | | | Calc-silicate rocks (protolith = marls) | | | | | |
|--|--------|--------|--------|--------|--------|---|--------|--------|--------|--------|--------|
| Sample | 14-38a | 10-38a | 07-40 | 15-46 | 13-38a | 12-64b | 12-12a | 10-4 | 14-53c | 14-17 | 12-65 |
| SiO ₂ | 69.93 | 69.82 | 71.00 | 79.12 | 69.16 | 72.05 | 70.14 | 72.37 | 73.48 | 62.92 | 66.13 |
| TiO ₂ | 0.56 | 0.48 | 0.61 | 0.46 | 0.66 | 0.57 | 0.64 | 0.57 | 0.33 | 0.48 | 0.63 |
| Al ₂ O ₃ | 10.82 | 10.68 | 11.12 | 6.86 | 11.13 | 8.00 | 8.11 | 7.83 | 5.70 | 8.09 | 8.25 |
| FeO _{tot} | 6.61 | 6.44 | 5.22 | 2.74 | 5.64 | 3.26 | 3.54 | 3.19 | 2.56 | 4.05 | 3.81 |
| MnO | 0.11 | 0.13 | 0.08 | 0.07 | 0.11 | 0.05 | 0.06 | 0.04 | 0.04 | 0.01 | 0.07 |
| MgO | 4.36 | 5.45 | 3.71 | 3.42 | 3.78 | 2.71 | 3.43 | 3.30 | 4.45 | 5.59 | 4.29 |
| CaO | 3.20 | 3.62 | 5.13 | 5.12 | 7.22 | 9.04 | 9.21 | 9.49 | 11.77 | 13.14 | 13.55 |
| Na ₂ O | 1.02 | 0.48 | 1.72 | 1.12 | 0.49 | 1.26 | 1.21 | 1.06 | 0.43 | 1.15 | 1.35 |
| K ₂ O | 3.32 | 2.84 | 1.33 | 1.08 | 1.75 | 2.99 | 3.58 | 2.07 | 1.20 | 4.55 | 1.87 |
| P ₂ O ₅ | 0.08 | 0.05 | 0.08 | 0.01 | 0.06 | 0.06 | 0.07 | 0.06 | 0.04 | 0.02 | 0.06 |
| Total | 100.00 | 100.00 | 100.00 | 100.00 | 100.00 | 100.00 | 100.00 | 100.00 | 100.00 | 100.00 | 100.00 |
| CaO* | 1.02 | 0.48 | 1.72 | 1.12 | 0.49 | 1.26 | 1.21 | 1.06 | 0.43 | 1.15 | 1.35 |
| CaO _{carb} | 2.18 | 3.14 | 3.42 | 4.00 | 6.73 | 7.78 | 8.00 | 8.43 | 11.34 | 11.99 | 12.19 |
| Approximate protolith's mineral composition (vol%) | | | | | | | | | | | |
| Kao | 0.0 | 0.0 | 6.0 | 0.0 | 9.0 | 0.0 | 0.0 | 0.0 | 0.0 | 0.0 | 0.0 |
| Ill | 20.0 | 27.0 | 19.0 | 14.0 | 24.0 | 8.0 | 4.0 | 14.0 | 13.0 | 0.0 | 12.0 |
| FeChl | 11.0 | 11.0 | 9.0 | 5.0 | 10.0 | 6.0 | 6.0 | 5.0 | 4.0 | 7.0 | 6.0 |
| MgChl | 7.0 | 9.0 | 6.0 | 6.0 | 6.0 | 5.0 | 6.0 | 6.0 | 7.0 | 9.0 | 7.0 |
| Qz | 30.0 | 34.0 | 34.0 | 54.0 | 35.0 | 34.0 | 29.0 | 42.0 | 52.0 | 20.0 | 33.0 |
| Cal | 3.0 | 5.0 | 5.0 | 6.0 | 10.0 | 11.0 | 12.0 | 12.0 | 17.0 | 17.0 | 17.0 |
| Ab | 8.0 | 4.0 | 14.0 | 9.0 | 4.0 | 10.0 | 10.0 | 8.0 | 3.0 | 8.0 | 11.0 |
| Kfs | 17.0 | 8.0 | 0.0 | 1.0 | 0.0 | 21.0 | 28.0 | 9.0 | 2.0 | 35.0 | 9.0 |
| An | 4.0 | 2.0 | 7.0 | 5.0 | 2.0 | 5.0 | 5.0 | 4.0 | 2.0 | 4.0 | 5.0 |

CaO* = CaO from the silicate fraction; CaO_{carb} = CaO from the calcite fraction**Table 1b. Bulk compositions (mol%) of meta-sediments ranging from calc-silicate rocks to impure marbles**

| Calc-silicate rocks (protolith = marls) | | | | | | | | | | Impure marbles (protolith = impure limestones) | | |
|--|--------|--------|--------|--------|--------|--------|--------|--------|--------|---|--------|--------|
| Sample | 08-67 | 08-57 | 07-20 | 09-25 | 04-28 | 13-64 | 10-49c | 14-20a | 07-22 | 07-41 | 05-55 | 10-47b |
| SiO ₂ | 65.34 | 60.21 | 61.28 | 57.80 | 61.68 | 55.03 | 48.87 | 45.79 | 42.99 | 30.62 | 31.10 | 12.41 |
| TiO ₂ | 0.27 | 0.55 | 0.64 | 0.59 | 0.52 | 0.56 | 0.23 | 0.47 | 0.40 | 0.35 | 0.33 | 0.07 |
| Al ₂ O ₃ | 8.90 | 9.01 | 10.10 | 9.89 | 8.02 | 8.99 | 5.99 | 7.20 | 6.55 | 5.20 | 3.96 | 1.29 |
| FeO _{tot} | 2.21 | 4.54 | 4.72 | 4.84 | 3.57 | 4.45 | 3.47 | 3.43 | 3.33 | 2.84 | 2.02 | 1.37 |
| MnO | 0.04 | 0.07 | 0.07 | 0.09 | 0.08 | 0.06 | 0.10 | 0.08 | 0.06 | 0.05 | 0.13 | 0.03 |
| MgO | 2.81 | 5.05 | 4.54 | 5.77 | 3.23 | 5.50 | 7.29 | 6.76 | 6.12 | 5.92 | 5.43 | 7.10 |
| CaO | 15.11 | 16.33 | 16.79 | 18.32 | 18.95 | 21.16 | 30.01 | 33.81 | 37.61 | 53.53 | 54.79 | 76.91 |
| Na ₂ O | 3.57 | 1.04 | 0.55 | 1.25 | 1.56 | 1.88 | 1.91 | 1.22 | 0.88 | 0.61 | 1.45 | 0.03 |
| K ₂ O | 1.74 | 3.14 | 1.24 | 1.40 | 2.33 | 2.33 | 2.07 | 1.19 | 2.01 | 0.85 | 0.75 | 0.75 |
| P ₂ O ₅ | 0.03 | 0.05 | 0.07 | 0.04 | 0.06 | 0.04 | 0.06 | 0.05 | 0.04 | 0.02 | 0.03 | 0.03 |
| Total | 100.00 | 100.00 | 100.00 | 100.00 | 100.00 | 100.00 | 100.00 | 100.00 | 100.00 | 100.00 | 100.00 | 100.00 |
| CaO* | 3.57 | 1.04 | 0.55 | 1.25 | 1.56 | 1.88 | 1.91 | 1.22 | 0.88 | 0.61 | 1.45 | 0.03 |
| CaO _{carb} | 11.54 | 15.29 | 16.24 | 17.08 | 17.39 | 19.28 | 28.11 | 32.59 | 36.73 | 52.92 | 53.34 | 76.88 |
| Approximate protolith's mineral composition (vol%) | | | | | | | | | | | | |
| Kao | 0.0 | 0.0 | 0.0 | 0.0 | 0.0 | 0.0 | 0.0 | 0.0 | 0.0 | 0.0 | 0.0 | 0.0 |
| Ill | 0.0 | 11.0 | 26.0 | 20.0 | 7.0 | 5.0 | 5.0 | 8.0 | 5.0 | 7.0 | 1.0 | 0.0 |
| FeChl | 4.0 | 7.0 | 8.0 | 8.0 | 6.0 | 7.0 | 5.0 | 5.0 | 5.0 | 4.0 | 3.0 | 2.0 |
| MgChl | 5.0 | 8.0 | 7.0 | 9.0 | 5.0 | 9.0 | 11.0 | 10.0 | 9.0 | 8.0 | 7.0 | 9.0 |
| Qz | 23.0 | 22.0 | 28.0 | 24.0 | 26.0 | 16.0 | 24.0 | 17.0 | 14.0 | 10.0 | 12.0 | 5.0 |
| Cal | 17.0 | 21.0 | 22.0 | 24.0 | 25.0 | 26.0 | 39.0 | 43.0 | 46.0 | 63.0 | 65.0 | 84.0 |
| Ab | 25.0 | 8.0 | 6.0 | 10.0 | 11.0 | 14.0 | 11.0 | 9.0 | 6.0 | 4.0 | 8.0 | 0.0 |
| Kfs | 13.0 | 19.0 | 0.0 | 0.0 | 14.0 | 16.0 | 0.0 | 4.0 | 12.0 | 2.0 | 0.0 | 0.0 |
| An | 13.0 | 4.0 | 3.0 | 5.0 | 6.0 | 7.0 | 5.0 | 4.0 | 3.0 | 2.0 | 4.0 | 0.0 |

CaO* = CaO from the silicate fraction; CaO_{carb} = CaO from the calcite fraction

Table 1c. Bulk compositions (mol%) of metapelites

| Metapelites s.s. from the LHS and GHS, Nepal Himalaya | | | | | | | | | | | |
|---|------------------------|------------------------|------------------------|-----------------------|-----------------------|-----------------------|------------------------|-----------------------|-----------------------|-----------------------|-----------------------|
| Sample | 14-27a ^[10] | 14-44a ^[10] | 14-61b ^[10] | 14-71 ^[10] | 14-52 ^[10] | 14-03 ^[10] | 14-25b ^[10] | 14-24 ^[10] | 06-02 ^[11] | 06-69 ^[11] | 06-29 ^[11] |
| SiO ₂ | 67.37 | 68.05 | 67.98 | 75.57 | 71.00 | 71.26 | 64.44 | 69.39 | 70.54 | 74.84 | 75.32 |
| TiO ₂ | 0.62 | 0.53 | 0.53 | 0.60 | 0.95 | 0.69 | 0.62 | 0.60 | 0.53 | 0.91 | 0.64 |
| Al ₂ O ₃ | 16.40 | 16.24 | 16.22 | 11.63 | 8.91 | 13.82 | 17.94 | 13.75 | 14.75 | 14.08 | 11.77 |
| FeO _{tot} | 6.59 | 4.75 | 4.75 | 5.49 | 7.25 | 6.10 | 7.76 | 6.01 | 4.17 | 4.32 | 4.70 |
| MnO | 0.15 | 0.12 | 0.12 | 0.12 | 0.07 | 0.20 | 0.24 | 0.21 | 0.29 | 0.04 | 0.12 |
| MgO | 1.96 | 3.18 | 3.18 | 1.74 | 6.63 | 2.85 | 3.08 | 2.54 | 3.07 | 2.30 | 2.37 |
| CaO | 0.88 | 0.84 | 0.84 | 0.32 | 0.61 | 0.45 | 0.57 | 3.22 | 1.30 | 0.09 | 0.52 |
| Na ₂ O | 0.80 | 1.76 | 1.76 | 1.00 | 1.83 | 0.72 | 1.79 | 0.71 | 2.36 | 0.44 | 1.77 |
| K ₂ O | 5.23 | 4.63 | 4.63 | 3.53 | 2.75 | 3.91 | 3.57 | 3.58 | 3.00 | 2.97 | 2.79 |
| P ₂ O ₅ | - | - | - | - | - | - | - | - | - | - | - |
| Total | 100.00 | 100.10 | 100.00 | 100.00 | 100.00 | 100.00 | 100.00 | 100.00 | 100.00 | 100.00 | 100.00 |
| CaO* | 0.80 | 3.18 | 2.16 | 1.74 | 6.63 | 2.85 | 3.05 | 0.71 | 2.93 | 2.20 | 2.30 |
| CaO _{carb} | 0.08 | 0.00 | 0.00 | 0.00 | 0.00 | 0.00 | 0.00 | 2.51 | 0.00 | 0.00 | 0.00 |

Approximate protolith's mineral composition (vol%)

| | | | | | | | | | | | |
|-------|------|------|------|------|------|------|------|------|------|------|------|
| Kao | 0.0 | 0.0 | 0.0 | 0.0 | 0.0 | 0.0 | 5.0 | 0.0 | 0.0 | 9.0 | 0.0 |
| Ill | 45.0 | 43.0 | 12.0 | 32.0 | 6.0 | 41.0 | 49.0 | 42.0 | 39.0 | 42.0 | 33.0 |
| FeChl | 11.0 | 7.8 | 11.0 | 10.0 | 13.0 | 11.0 | 13.0 | 10.0 | 7.0 | 7.0 | 8.0 |
| MgChl | 3.0 | 5.0 | 4.0 | 3.0 | 12.0 | 5.0 | 5.0 | 4.0 | 5.0 | 4.0 | 4.0 |
| Qz | 16.0 | 14.0 | 21.0 | 35.0 | 30.0 | 26.0 | 12.0 | 27.0 | 23.0 | 35.0 | 34.0 |
| Cal | 0.0 | 0.0 | 0.0 | 0.0 | 0.0 | 0.0 | 0.0 | 3.0 | 0.0 | 0.0 | 0.0 |
| Ab | 6.0 | 14.0 | 28.0 | 8.0 | 15.0 | 6.0 | 14.0 | 6.0 | 19.0 | 3.0 | 14.0 |
| Kfs | 3.0 | 3.2 | 3.0 | 1.0 | 3.0 | 2.0 | 2.0 | 3.0 | 5.0 | 0.0 | 2.0 |
| An | 16.0 | 13.0 | 21.0 | 11.0 | 21.0 | 9.0 | 0.0 | 5.0 | 2.0 | 0.0 | 5.0 |

[10] Metapelites from the LHS and GHS: Rapa et al., 2016. [11] Metapelites from the LHS and GHS: Groppo et al., 2009.

CaO* = CaO from the silicate fraction; CaO_{carb} = CaO from the calcite fraction

Table 1d. Bulk compositions (mol%) of pelites and metapelites

| Pelites s.s. and metapelites s.s. from the literature | | | | | | | | | |
|---|---------------------|---------------------|-------------------------------|--|---|---|---|--|---|
| Sample | NASC ^[1] | PAAS ^[2] | Av. pelites ^[3] | Av. pelagic clays ^[4] | Av. Archean Shales ^[5] | Av. Proteroz. Shales ^[6] | Av. Phaneroz. Shales ^[7] | Av. low- grade metap. ^[8] | Av. medium- grade metap. ^[9] |
| SiO ₂ | 70.42 | 71.11 | 70.18 | 67.30 | 69.95 | 73.39 | 72.31 | 77.89 | 64.61 |
| TiO ₂ | 0.66 | 0.85 | 0.67 | 0.72 | 0.54 | 0.56 | 0.70 | 0.82 | 0.91 |
| Al ₂ O ₃ | 10.91 | 12.61 | 11.69 | 12.00 | 11.84 | 11.99 | 11.92 | 6.34 | 13.66 |
| FeO _{tot} | 5.18 | 6.15 | 6.44 | 9.15 | 7.23 | 5.49 | 5.60 | 6.78 | 8.04 |
| MnO | 0.23 | 0.00 | 0.09 | 0.00 | 0.00 | 0.00 | 0.00 | 0.00 | 0.18 |
| MgO | 4.58 | 3.71 | 4.67 | 6.22 | 6.64 | 3.81 | 3.90 | 4.05 | 5.53 |
| CaO | 4.08 | 1.58 | 1.81 | 0.95 | 0.79 | 0.88 | 1.58 | 0.22 | 1.96 |
| Na ₂ O | 1.19 | 1.32 | 1.75 | 1.55 | 0.76 | 1.19 | 1.21 | 0.97 | 2.07 |
| K ₂ O | 2.75 | 2.67 | 2.70 | 2.11 | 2.25 | 2.69 | 2.78 | 2.93 | 3.04 |
| P ₂ O ₅ | - | - | - | - | - | - | - | - | - |
| Total | 100.00 | 100.00 | 100.00 | 100.00 | 100.00 | 100.00 | 100.00 | 100.00 | 100.00 |
| CaO* | 1.19 | 1.32 | 1.75 | 6.22 | 0.76 | 0.88 | 1.21 | 4.05 | 5.53 |
| CaO _{carb} | 2.89 | 0.26 | 0.06 | 0.00 | 0.03 | 0.00 | 0.37 | 0.00 | 0.00 |

Approximate protolith's mineral composition (vol%)

| | | | | | | | | | |
|-------|------|------|------|------|------|------|------|------|------|
| Kao | 0.0 | 0.0 | 0.0 | 0.0 | 0.0 | 0.0 | 0.0 | 0.0 | 0.0 |
| Ill | 23.0 | 32.0 | 20.0 | 26.0 | 32.0 | 32.0 | 28.0 | 0.3 | 23.0 |
| FeChl | 9.0 | 11.0 | 11.0 | 16.0 | 13.0 | 10.0 | 10.0 | 12.3 | 14.0 |
| MgChl | 8.0 | 6.0 | 8.0 | 11.0 | 11.0 | 7.0 | 7.0 | 7.2 | 9.0 |
| Qz | 31.0 | 31.0 | 28.0 | 27.0 | 35.0 | 33.0 | 32.0 | 45.1 | 17.0 |
| Cal | 4.0 | 0.0 | 0.0 | 0.0 | 0.0 | 0.0 | 1.0 | 0.0 | 0.0 |
| Ab | 10.0 | 11.0 | 14.0 | 13.0 | 6.0 | 10.0 | 10.0 | 8.2 | 17.0 |
| Kfs | 5.0 | 5.0 | 7.0 | 4.0 | 3.0 | 4.0 | 5.0 | 0.9 | 8.0 |
| An | 10.0 | 4.0 | 12.0 | 3.0 | 0.0 | 4.0 | 7.0 | 26.0 | 12.0 |

[1] NASC "North American Shale Composite": Gromet et al., 1984. [2] PAAS "Post-Archean Australian Shale: Taylor & McLennan, 1985. [3] Average pelites: Ague, 1991; [4] Average pelagic clays: Carmichael, 1989. [5] Average Archean Shales: Condie, 1993. [6] Average Proterozoic Shales: Condie, 1993. [7] Average Phanerozoic Shales: Condie, 1993. [8] Average low-grade metapelites: Shaw, 1956. [9] Average amphibolite-facies metapelites: Ague, 1991.

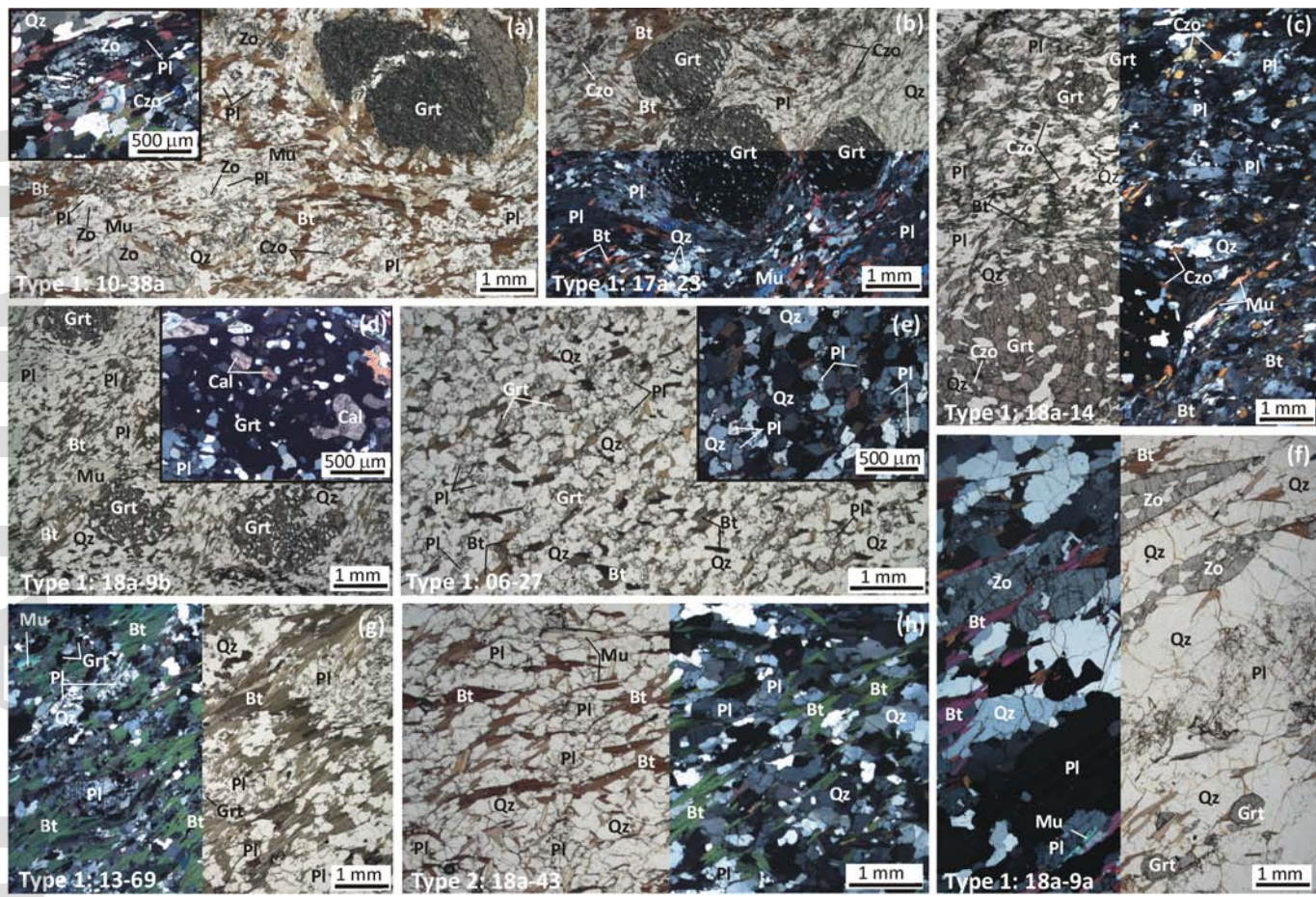
CaO* = CaO from the silicate fraction; CaO_{carb} = CaO from the calcite fraction

Table 2. Model bulk compositions (mol%)

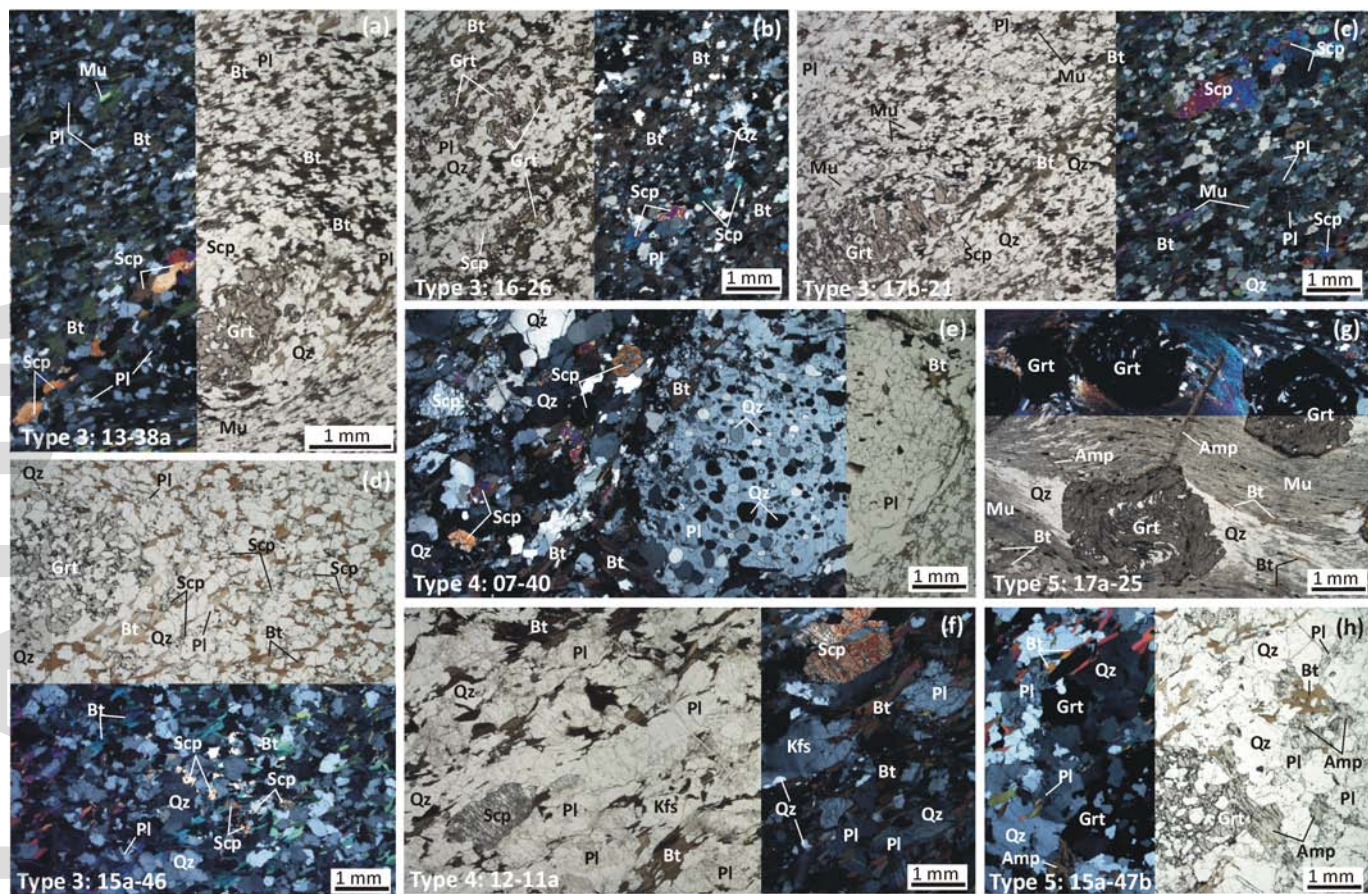
| Sample | Ca0 | Ca3 | Ca6 | Ca9 | Ca0_ highMg | Ca3_ highMg | Ca6_ highMg | Ca9_ highMg | Ca0_ lowNa | Ca3_ lowNa | Ca6_ lowNa | Ca9_ lowNa | Ca0_ highNa | Ca3_ highNa | Ca6_ highNa | Ca9_ highNa |
|--------------------------------|-------|-------|-------|-------|----------------|----------------|----------------|----------------|---------------|---------------|---------------|---------------|----------------|----------------|----------------|----------------|
| SiO ₂ | 72.2 | 70.0 | 68.2 | 66.9 | 72.2 | 70.0 | 68.2 | 66.9 | 73.2 | 70.9 | 69.1 | 67.7 | 71.4 | 69.1 | 67.3 | 66.0 |
| TiO ₂ | 0.7 | 0.7 | 0.7 | 0.7 | 0.7 | 0.7 | 0.7 | 0.7 | 0.7 | 0.7 | 0.7 | 0.7 | 0.7 | 0.7 | 0.7 | 0.7 |
| Al ₂ O ₃ | 11.1 | 10.8 | 10.5 | 10.3 | 11.1 | 10.8 | 10.5 | 10.3 | 11.3 | 10.9 | 10.7 | 10.4 | 11.0 | 10.7 | 10.4 | 10.2 |
| FeO _{tot} | 6.2 | 6.0 | 5.8 | 5.7 | 4.3 | 4.2 | 4.1 | 4.0 | 6.3 | 6.1 | 5.9 | 5.8 | 6.1 | 5.9 | 5.8 | 5.7 |
| MnO | 0.1 | 0.1 | 0.1 | 0.1 | 0.1 | 0.1 | 0.1 | 0.1 | 0.1 | 0.1 | 0.1 | 0.1 | 0.1 | 0.1 | 0.1 | 0.1 |
| MgO | 4.3 | 4.2 | 4.1 | 4.0 | 6.2 | 6.0 | 5.8 | 5.7 | 4.4 | 4.3 | 4.1 | 4.1 | 4.3 | 4.2 | 4.0 | 4.0 |
| CaO | 1.0 | 4.0 | 6.4 | 8.3 | 1.0 | 4.0 | 6.4 | 8.3 | 1.0 | 4.0 | 6.5 | 8.4 | 1.0 | 3.9 | 6.4 | 8.2 |
| Na ₂ O | 1.9 | 1.8 | 1.8 | 1.7 | 1.9 | 1.8 | 1.8 | 1.7 | 0.5 | 0.5 | 0.5 | 0.5 | 3.0 | 3.0 | 3.0 | 3.0 |
| K ₂ O | 2.5 | 2.4 | 2.3 | 2.3 | 2.5 | 2.4 | 2.3 | 2.3 | 2.5 | 2.4 | 2.4 | 2.3 | 2.5 | 2.4 | 2.3 | 2.3 |
| Total | 100.0 | 100.0 | 100.0 | 100.0 | 100.0 | 100.0 | 100.0 | 100.0 | 100.0 | 100.0 | 100.0 | 100.0 | 100.0 | 100.0 | 100.0 | 100.0 |
| CaO* | 1.0 | 1.8 | 1.8 | 1.7 | 1.0 | 1.8 | 1.8 | 1.7 | 1.0 | 0.5 | 0.5 | 0.5 | 1.0 | 3.0 | 3.0 | 3.0 |
| CaO _{carb} | 0.0 | 2.2 | 4.7 | 6.5 | 0.0 | 2.2 | 4.7 | 6.5 | 0.0 | 3.5 | 6.0 | 7.9 | 0.0 | 1.0 | 3.4 | 5.2 |

Approximate protolith's mineral composition (vol%)

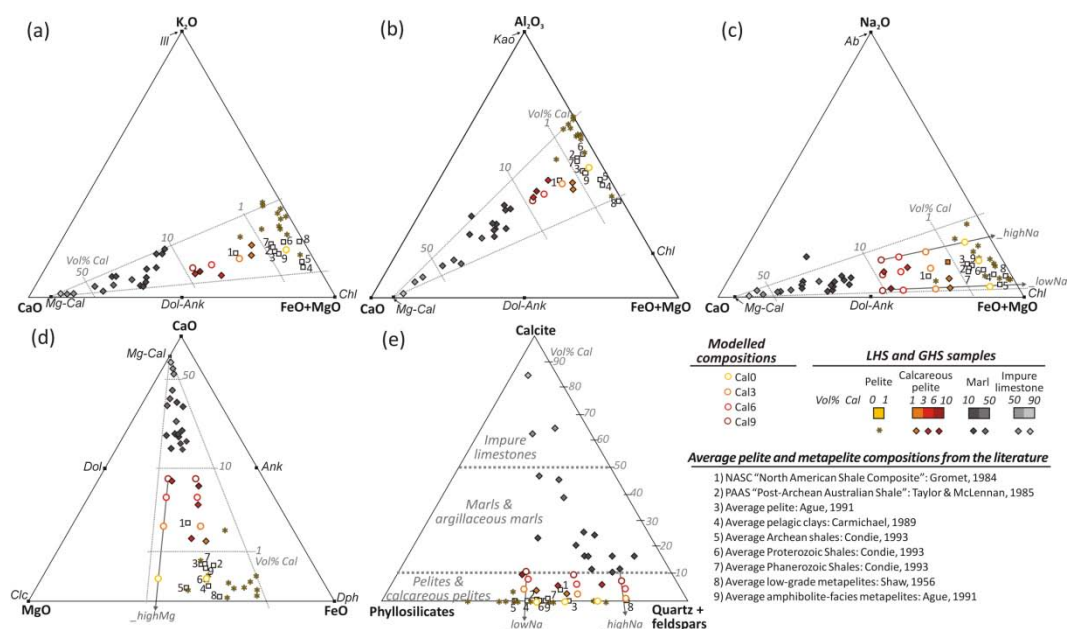
| | | | | | | | | | | | | | | | | |
|-------|----|----|----|----|----|----|----|----|----|----|----|----|----|----|----|----|
| Kao | 0 | 0 | 0 | 0 | 0 | 0 | 0 | 0 | 0 | 0 | 0 | 0 | 0 | 0 | 0 | 0 |
| Ill | 22 | 17 | 16 | 15 | 22 | 17 | 16 | 15 | 31 | 33 | 31 | 30 | 15 | 2 | 1 | 1 |
| FeChl | 11 | 10 | 10 | 10 | 7 | 7 | 7 | 7 | 11 | 11 | 10 | 10 | 11 | 10 | 10 | 10 |
| MgChl | 7 | 7 | 7 | 7 | 11 | 10 | 10 | 10 | 8 | 7 | 7 | 7 | 7 | 7 | 7 | 7 |
| Qz | 31 | 29 | 30 | 28 | 31 | 1 | 30 | 28 | 38 | 37 | 36 | 35 | 26 | 24 | 22 | 20 |
| Cal | 0 | 3 | 6 | 9 | 0 | 3 | 6 | 9 | 0 | 5 | 9 | 11 | 0 | 1 | 5 | 8 |
| Ab | 16 | 15 | 14 | 14 | 16 | 15 | 14 | 14 | 4 | 4 | 4 | 4 | 24 | 24 | 24 | 23 |
| An | 4 | 7 | 7 | 7 | 4 | 7 | 7 | 7 | 4 | 2 | 2 | 2 | 4 | 12 | 12 | 12 |
| Kfs | 9 | 11 | 10 | 10 | 9 | 11 | 10 | 10 | 4 | 1 | 1 | 1 | 13 | 20 | 19 | 19 |



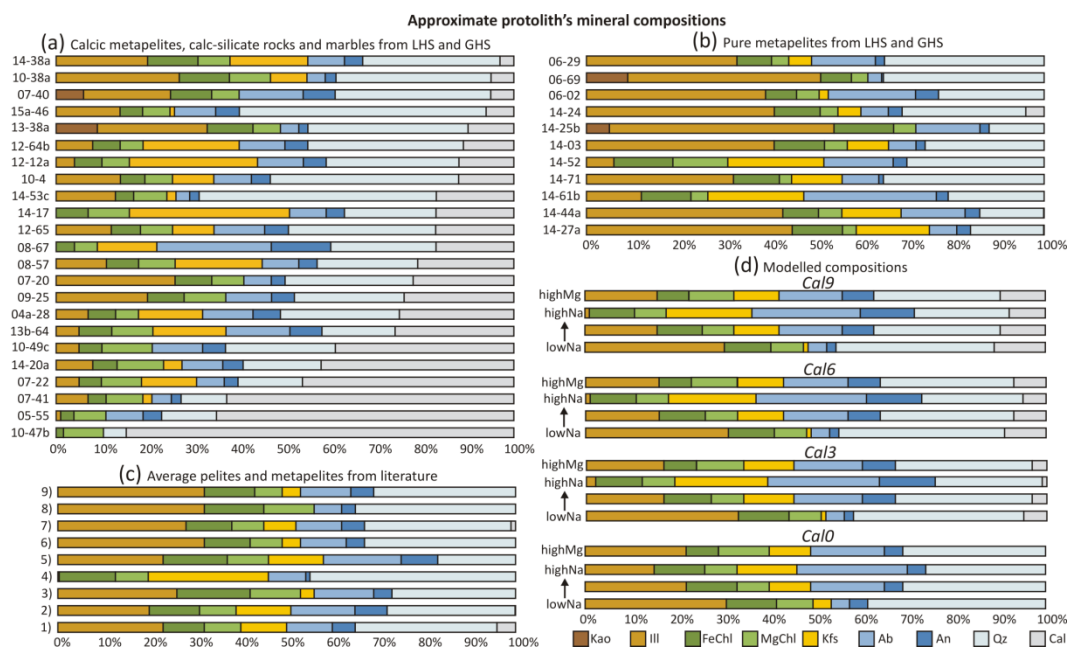
jmg_12568_f1.tif



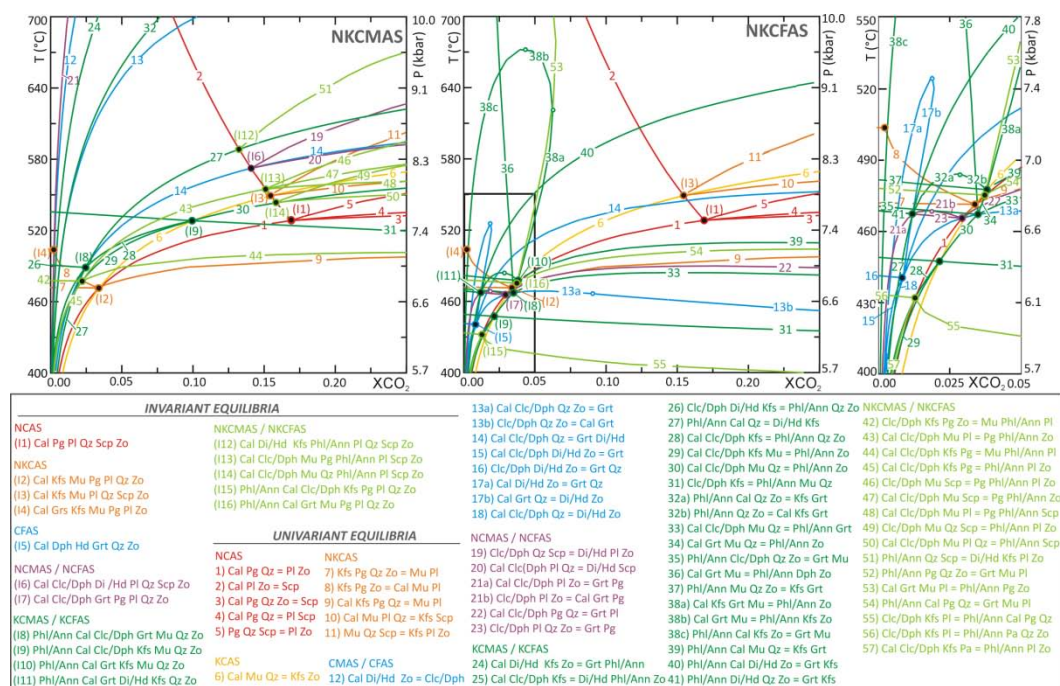
jmg_12568_f2.tif



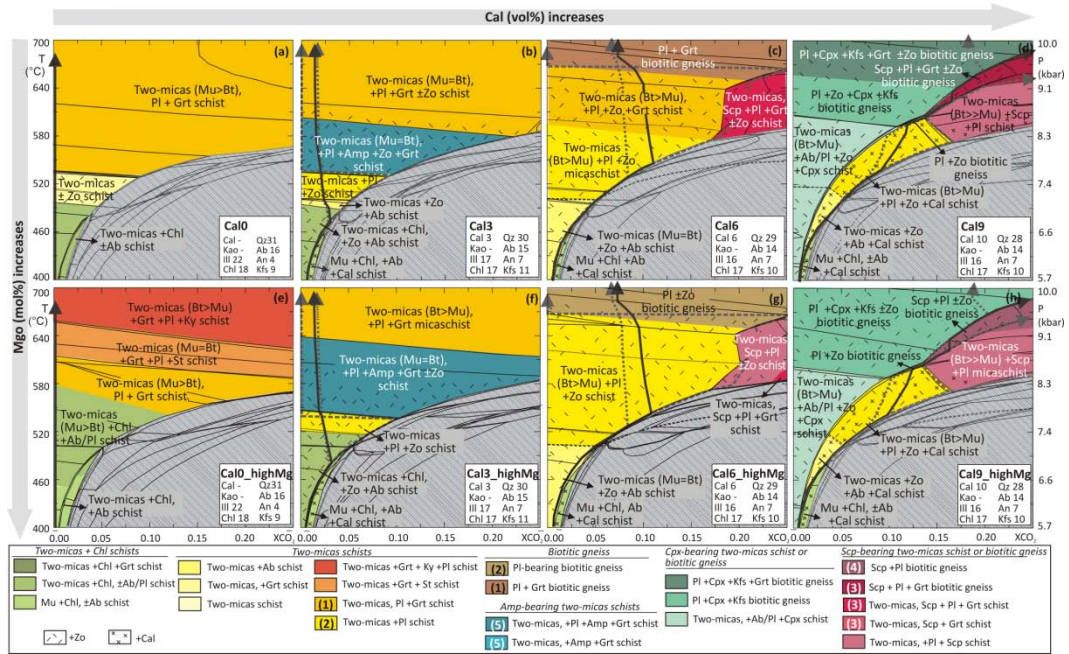
jmg_12568_f3.tif



jmg_12568_f4.tif

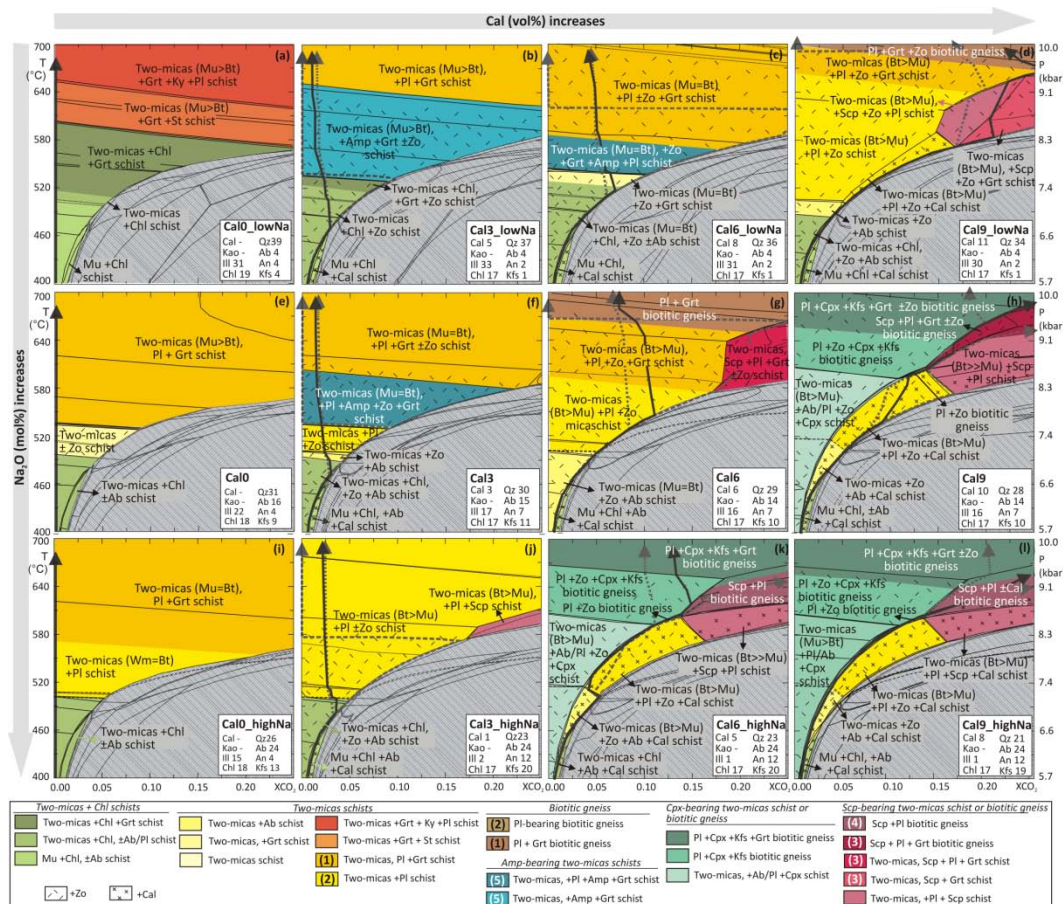


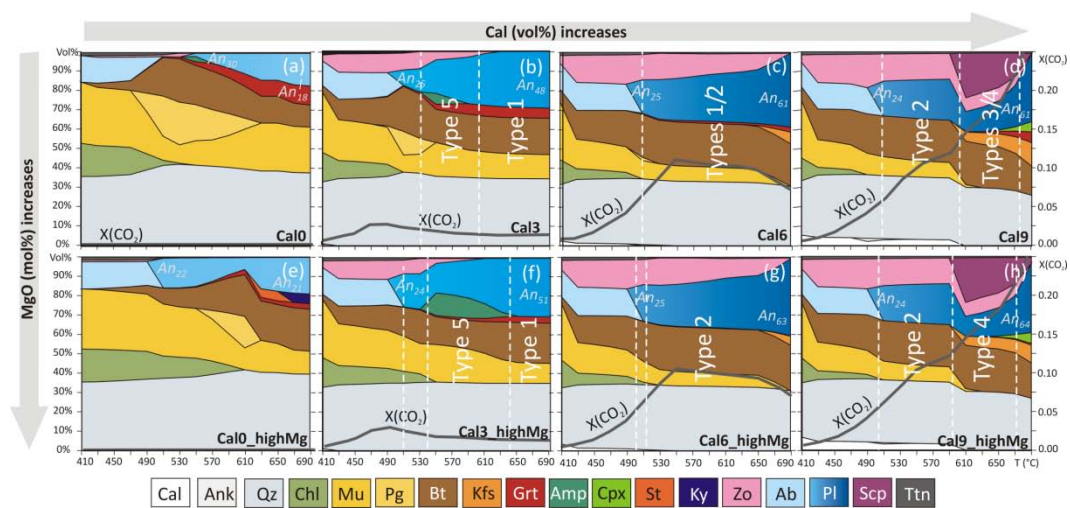
jmg_12568_f5.tif



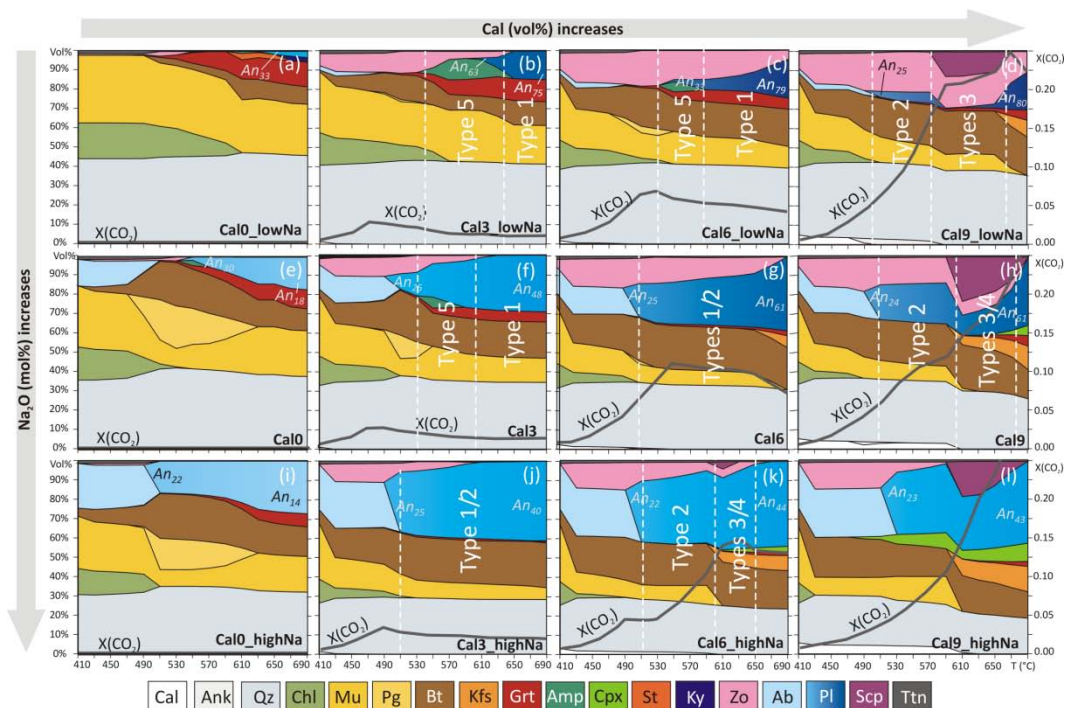
jmg_12568_f6.tif

jmg_12568_f7.tif

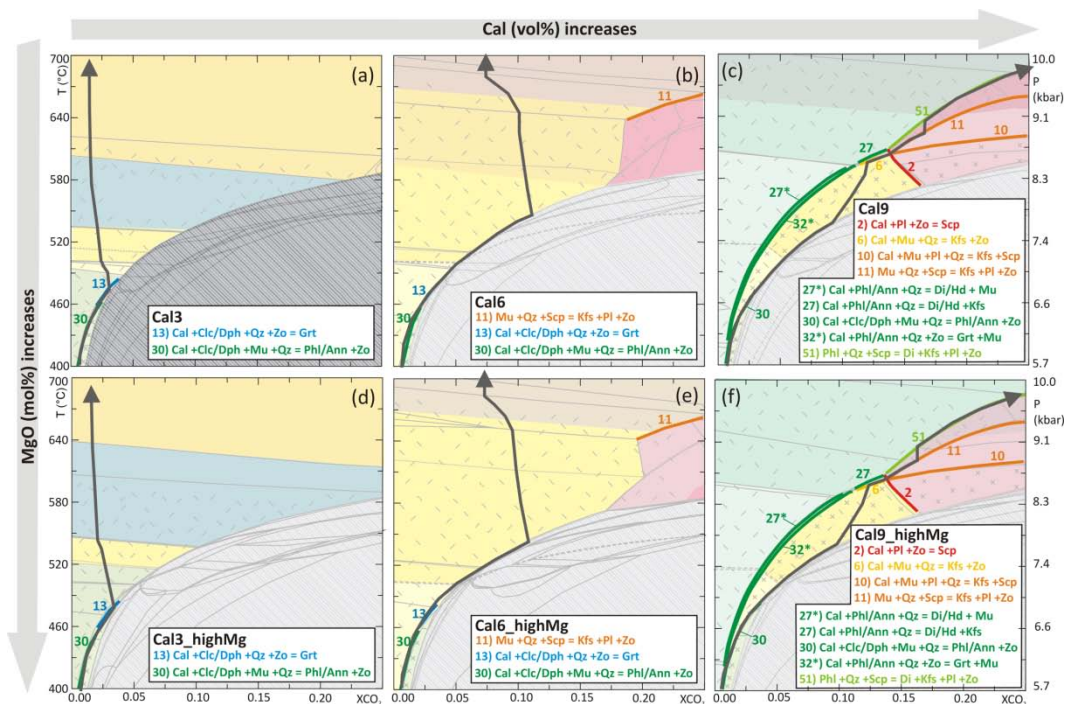




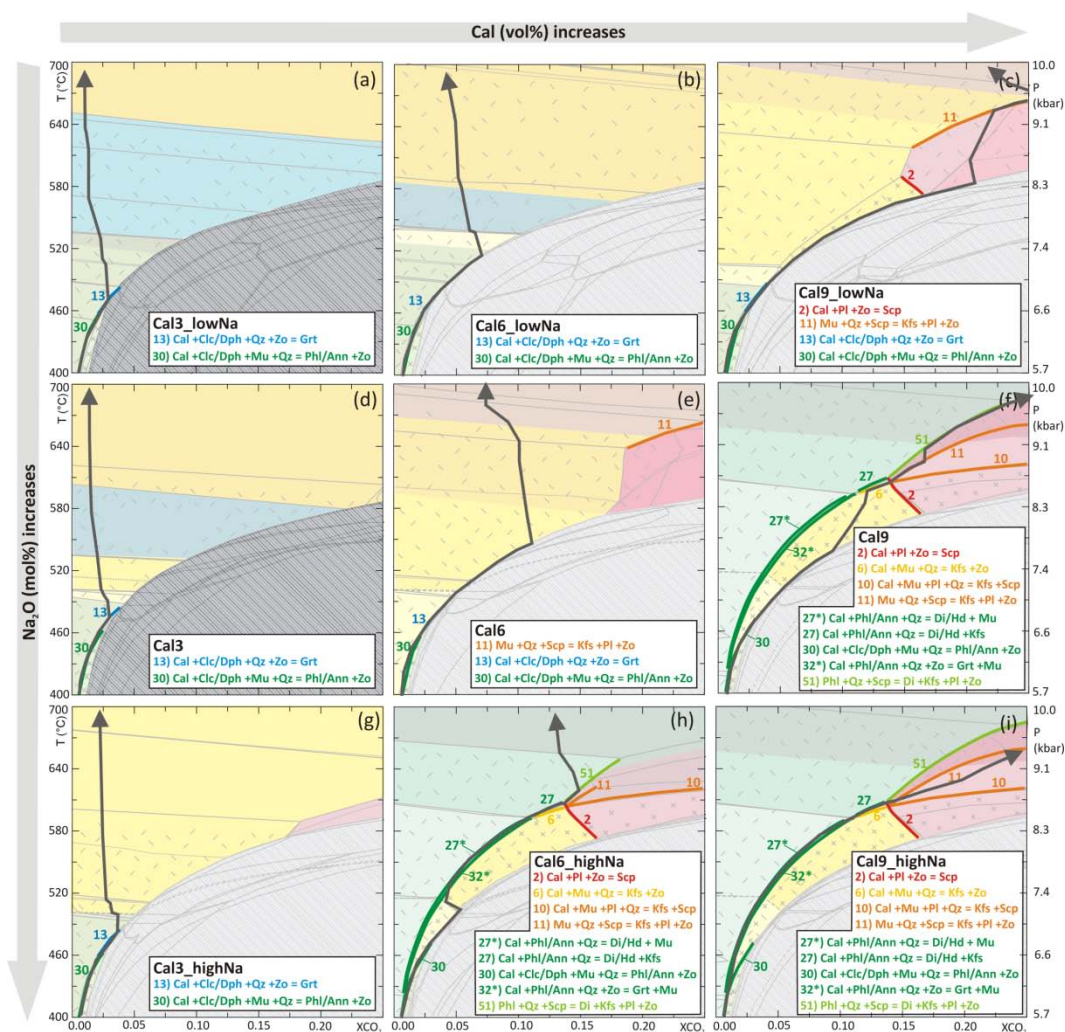
jmg_12568_f8.tif



jmg_12568_f9.tif



jmg_12568_f10.tif



jmg_12568_f11.tif